INSTITUTE OF PHYSICS PUBLISHING JOURNAL OF PHYSICS: CONDENSED MATTER

J. Phys.: Condens. Matter **15** (2003) R1395–R1428 PII: S0953-8984(03)62902-4

TOPICAL REVIEW

Electrical pulse measurement, inelastic relaxation, and non-equilibrium transport in a quantum dot

T Fujisawa[1], **D G Austing**[1,2], **Y Tokura**[1], **Y Hirayama**[1,3] **and S Tarucha**[1,4,5]

[1] NTT Basic Research Laboratories, NTT Corporation, 3-1 Morinosato-Wakamiya, Atsugi 243-0198, Japan
[2] Institute of Microstructural Science M23A, National Research Council of Canada, Ottawa, ON K1A 0R6, Canada
[3] CREST, 4-1-8 Honmachi, Kawaguchi 331-0012, Japan
[4] University of Tokyo, Bunkyo-ku, Tokyo 113-0033, Japan
[5] ERATO Mesoscopic Correlation Project, 3-1 Morinosato-Wakamiya, Atsugi 243-0198, Japan

E-mail: fujisawa@will.brl.ntt.co.jp

Received 30 April 2003
Published 8 August 2003
Online at stacks.iop.org/JPhysCM/15/R1395

Abstract

We review electrical pulse experiments carried out to probe inelastic energy relaxation processes and related non-equilibrium transport characteristics of quantum dots (QDs) in the Coulomb blockade (CB) regime. In contrast to the relatively short momentum relaxation time ($\sim$10 ns) that can be understood on the basis of acoustic phonon emission, the spin-flip relaxation time is found to be extremely long ($\sim$200 μs). The spin relaxation process in our QDs is actually dominated by a cotunnelling process, and thus the intrinsic spin relaxation should have a longer relaxation time. The long relaxation time is discussed in terms of potential applications to spin-based quantum information storage. On the other hand, the extremely long spin relaxation process can induce considerable fluctuation of the spin, charge, and total energy of the QD. The absence of efficient spin relaxation processes can cause highly non-equilibrium transport, which actually 'breaks down' the single-electron tunnelling scheme. The non-equilibrium effects must be considered when electrons and spins are manipulated in the CB regime.

(Some figures in this article are in colour only in the electronic version)

Contents

1. Introduction

Electron spins in semiconductors have attracted much attention in spin-based electronics, in which the spin degree of freedom can be utilized for future electronic devices, as well as spin-based quantum information processing, which is expected to provide a powerful quantum computing scheme [1, 2]. A quantum dot (QD), which accommodates a tunable number of electrons, shows many spin dependent phenomena [3]. Coulomb and exchange interactions between electrons inside QDs induce spin-polarized states [4–6]. Strong tunnel coupling with electrodes screens localized spins in a QD, and this gives rise to Kondo resonant tunnelling current in the Coulomb blockade (CB) regime [7]. The dynamical characteristics of spin states in QDs are of growing interest for developing spin-based information processing. Dissipation and decoherence are fundamental aspects of quantum dynamics. QDs are expected to provide long dissipation and decoherence time due to the localized nature of the electronic states [8]. However, electron spin in a realistic QD has an unavoidable coupling to the nuclear spin (hyperfine coupling), the orbital degree of freedom of the electron (spin–orbit coupling), the lattice vibration mode (spin–phonon coupling), the electromagnetic field (dipole magnetic coupling), etc [8, 9]. In addition, a practical QD may suffer from extrinsic effects, such as coupling to conduction electrons in the vicinity of the QD, extra spin–orbit coupling due to the heterostructure interface or impurities, and the influence from fluctuations of the electric or magnetic field. Consequently, it is important to know how long spin information can be preserved in practical QDs.

Spin relaxation in QDs has been studied mainly by optical orientation techniques, in which spin-polarized electrons, consistent with the optical selection rules, are excited between the valence band and the conduction band in III–V semiconductors [10–12]. However, this scheme is complicated by the generation of holes in the valence band, which can give rise to unwanted processes. Alternative techniques based on electrical measurements in the CB regime have successfully proved inelastic spin relaxation, and this is reviewed in our article. First, we introduce electrical pulse measurements to investigate the energy relaxation in a QD in the CB regime. Next, we discuss the momentum and spin relaxation processes observed

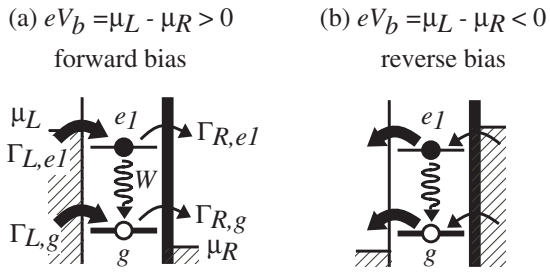

Figure 1. Schematic energy diagrams of the dc transport (a) in forward bias and (b) in reverse bias. The GS, g, and first ES, e_1, are in the transport window. Thick (thin) arrows indicate tunnelling transitions with higher (lower) rates. Energy relaxation from e_1 to g is considered.

in one- and two-electron QDs. Spin conservation during the relaxation processes is clearly observed. The transition is allowed for by a simple phonon emission process, but is strongly forbidden if the spin is changed. Lastly, highly non-equilibrium transport in the absence of an efficient spin relaxation process is described. Excess energy accumulated in long-lived spin states can 'break down' the widely accepted single-electron tunnelling (SET) scheme. The spin blockade effect and associated non-equilibrium transport are also discussed.

2. Electrical measurements carried out to determine energy relaxation time

We first describe the electrical measurements used to determine tunnelling rates through barriers as well as the rate of energy relaxation from an excited state (ES) to a ground state (GS) in a QD. We consider a general QD in the CB regime where the number of electrons in the QD is a fixed integer, N [13]. When a gate voltage is instantly changed to force the QD from one CB region at $N = N_0$ (N_0+1) to another at $N = N_0+1$ (N_0), one electron is injected into (extracted from) the QD. Injection and extraction can be performed on a timescale given approximately by the inverse of the barrier tunnelling rates, Γ^{-1}, which can be varied over a wide range from $\sim$1 ps to $\sim$1 μs for typical QDs. Moreover, an electron can be (sometimes selectively) injected into, or extracted from, the GS or ESs by adjusting external voltages. Repeatedly applying voltage pulses pushes the system out of equilibrium, and by measuring the time-integrated non-equilibrium transient current we can determine the energy relaxation time or the tunnelling rates.

2.1. The dc measurement

We now discuss to what degree conventional dc measurements can shed light on relaxation/tunnelling dynamics. We consider a simple situation where the GS, g, and the first ES, e_1, are in the transport window between the left- and right-lead chemical potentials (μ_L and μ_R), and consider the energy relaxation process, whose rate is W, from the ES to the GS (figures 1(a) and (b)). Each state (i = g, e_1) is coupled to the left and right lead with tunnelling rates $\Gamma_{L,i}$ and $\Gamma_{R,i}$, respectively. We consider strongly asymmetric barriers, $\Gamma_{L,i} \gg \Gamma_{R,i}$, and define the forward bias direction as that where an electron is injected from the thinner barrier ($\Gamma_{L,i}$) and ejected through the thick barrier ($\Gamma_{R,i}$), throughout this article. As shown below, current in forward (reverse) bias is sensitive (insensitive) to the relaxation rate.

The current through the dot can be simply estimated from the rate equations considering all the processes described by the arrows in figures 1(a) and (b). At sufficiently low temperature

and relatively high source–drain voltage, an electron sequentially travels through the states from the left electrode to the right electrode, while the backward travelling from the right to the left is suppressed. Thus, as long as the states of interest are in the transport window, the current is insensitive to the energies and the applied source–drain voltage if we assume energy independent tunnelling rates. This saturated current yields

$$I_{\mathrm{f}} = \frac{e\Gamma_{\mathrm{R,g}}(\Gamma_{\mathrm{L,g}} + \Gamma_{\mathrm{L,e_1}})(\Gamma_{\mathrm{R,e_1}} + W)}{\Gamma_{\mathrm{L,g}}(\Gamma_{\mathrm{R,e_1}} + W) + \Gamma_{\mathrm{L,e_1}}(\Gamma_{\mathrm{R,g}} + W)} \tag{1}$$

for forward bias, and

$$I_{\mathrm{r}} = e(\Gamma_{\mathrm{R,g}} + \Gamma_{\mathrm{R,e_1}}) \tag{2}$$

for reverse bias [14]. The reverse bias current, I_{r}, is independent of W, since it is determined by the incoming tunnelling rates alone. Generally, I_{r} is given by the rate $\Gamma_{\mathrm{R},i}$ of tunnelling through the thick barrier to the ith empty state located in the transport window; $I_{\mathrm{r}} = e\sum\Gamma_{\mathrm{R},i}$. Thus I_{r} increases stepwise when an empty state enters the transport window. All the energy states and corresponding tunnelling rates can be measured in this way, unless the coupling to the leads $\Gamma_{\mathrm{R},i}$ is too weak.

In contrast, the current for forward bias (equation (1)) depends on W, since it is determined by the outgoing rates of tunnelling from QD states whose populations are affected by the relaxation. In the limit of fast relaxation, $W \gg \Gamma_{\mathrm{R},i}$, the current becomes

$$I_{\mathrm{f}} = e\Gamma_{\mathrm{R,g}}, \tag{3}$$

which is identical to the current through just the GS. In the opposite limit of slow relaxation, $W \ll \Gamma_{\mathrm{R},i}$,

$$I_{\mathrm{f}} = \frac{e\Gamma_{\mathrm{R,g}}\Gamma_{\mathrm{R,e_1}}(\Gamma_{\mathrm{L,g}} + \Gamma_{\mathrm{L,e_1}})}{\Gamma_{\mathrm{L,g}}\Gamma_{\mathrm{R,e_1}} + \Gamma_{\mathrm{L,e_1}}\Gamma_{\mathrm{R,g}}}, \tag{4}$$

which is different from equation (3) if $\Gamma_{\mathrm{R,g}} \neq \Gamma_{\mathrm{R,e_1}}$. Therefore, a current step appears at $\mu_{\mathrm{L}} = E_{\mathrm{e_1}}$ only when the relaxation rate is not much larger than the tunnelling rate. If more than two ESs are in the transport window, a similar argument can be constructed by considering W to be the sum of all the relaxation processes from the ESs to any lower-lying energy states [14, 15]. However, equation (1) is too complicated to use to estimate W from the dc characteristics alone.

2.2. Single-step pulse measurement

Next, we consider the case where a rectangular-shaped voltage pulse is applied to a gate electrode, as schematically shown in figures 2(a) and (b) [14]. The gate voltage, $V_{\mathrm{g}}(t)$, is switching instantaneously between the low-voltage state, V_{l}, and the high-voltage state, V_{h}. As in the case for the dc measurement scheme, we consider strongly asymmetric tunnelling barriers ($\Gamma_{\mathrm{L}} \gg \Gamma_{\mathrm{R}}$) and energy relaxation from the first ES to the GS. The polarity of the bias voltage is chosen such that an electron is injected through the thinner barrier at a fast rate Γ_{L}, and an electron is ejected through the thicker barrier at a slow rate Γ_{R} (forward bias).

First, we prepare the QD in the $(N_0 - 1)$-electron GS by setting the gate voltage to $V_{\mathrm{g}} = V_{\mathrm{l}}$ in the $N_0 - 1$ CB region for a sufficiently long period of time, $t_{\mathrm{l}} \gg \Gamma_{\mathrm{L}}^{-1}$ (figure 2(c)). In this situation, both the N_0-electron ES and the GS are energetically located above the chemical potential of the two electrodes, μ_{L} and μ_{R}. Then, the gate voltage is suddenly switched to $V_{\mathrm{g}} = V_{\mathrm{h}}$ in the N_0-electron CB region. The rise time of the voltage pulse should be comparable to or shorter than Γ_{L}^{-1} to see the following effects. The high voltage $V_{\mathrm{g}} = V_{\mathrm{h}}$ is adjusted such that only the N_0-electron ES is located between μ_{L} and μ_{R} (the transport

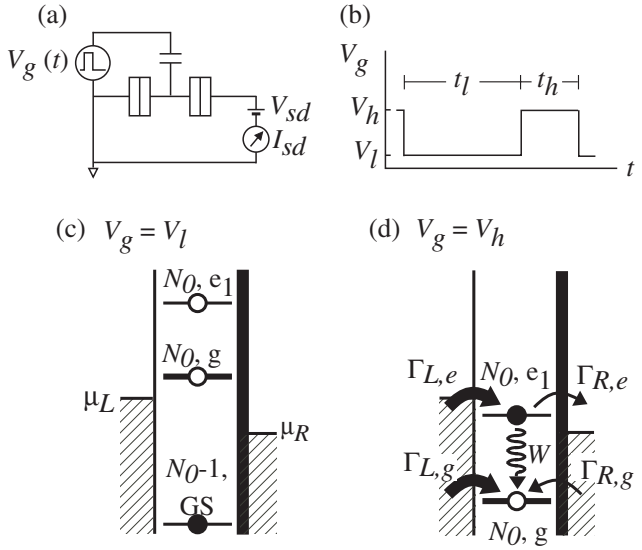

Figure 2. (a) A schematic diagram of the pulse measurement set-up. (b) The pulse waveform for the single-step pulse measurement. (c), (d) Schematic energy diagrams for the low-voltage and the high-voltage states respectively.

window), as shown in figure 2(d). First an electron enters either the N_0-electron ES or the GS with probabilities $\Gamma_{L,e}$ and $\Gamma_{L,g} + \Gamma_{R,g}$, respectively, but only one electron can enter the dot at a time. If an electron enters the ES, it can relax to the GS, or tunnel to the right electrode to give a net current. However, the transport is blocked once the GS is occupied (CB). Because of the strongly asymmetric barriers, $\Gamma_L \gg \Gamma_R$, an electron can stay in the ES for a relatively long time, $\sim\Gamma_R^{-1}$, during which relaxation may take place. The transport through the ES is terminated by a relaxation process. Therefore, transport in the forward bias is sensitive to the relaxation time.

This transient transport scheme can be considered to be a kind of pump and probe measurement. An electron is pumped into the ES within Γ_L^{-1} after a rising edge of the pulse, and then the electron in the ES is probed via the slower tunnelling rate Γ_R^{-1} in the high-voltage state. Note that a relatively large source–drain voltage, $|V_{sd}| \gg \hbar\Gamma_L$, has to be applied in order to eliminate backward tunnelling processes, such as tunnelling from the N_0-electron ES back to the left source electrode, which can degrade the relaxation time measurement.

To clarify this scheme, we analyse this non-equilibrium transport by using simple rate equations [16]. The non-equilibrium transport in the high-voltage state is described by

$$\begin{aligned} \frac{\mathrm{d}}{\mathrm{d}t}\rho_e &= \Gamma_{L,e}(1-\rho_e-\rho_g) - \Gamma_{R,e}\rho_e - W\rho_e, \\ \frac{\mathrm{d}}{\mathrm{d}t}\rho_g &= (\Gamma_{L,g}+\Gamma_{R,g})(1-\rho_e-\rho_g) + W\rho_e, \end{aligned} \tag{5}$$

in which all the tunnelling processes shown by arrows in figure 2(d) are taken into account. Here, ρ_e and ρ_g are the average electron numbers in the ES and the GS, respectively. $\rho_e = \rho_g = 0$ at $t = 0$, and $0 \leqslant \rho_e + \rho_g \leqslant 1$ is satisfied due to CB. The average number, $\langle n_h \rangle$, of tunnelling electrons that have passed through the QD during the high-voltage state is given by

$$\langle n_h \rangle = \int_{t=0}^{t_h} [\Gamma_{R,e}\rho_e - \Gamma_{R,g}(1-\rho_e-\rho_g)]\,\mathrm{d}t. \tag{6}$$

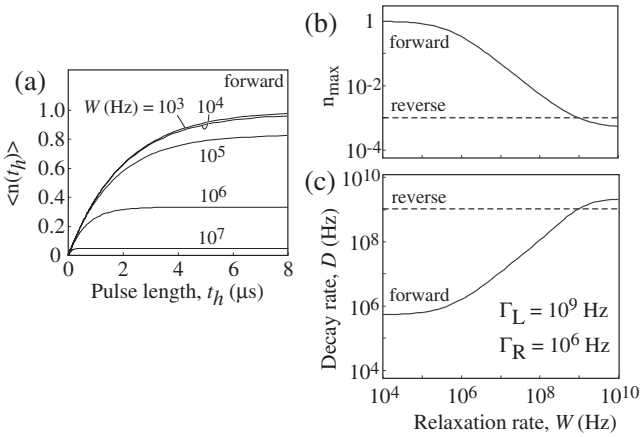

Figure 3. (a) The average number of tunnelling electrons, $\langle n(t_\mathrm{h})\rangle$, calculated for the single-step pulse scheme. Each curve is approximated by a single-exponential curve, whose parameters n_max and D are plotted in (b) and (c) respectively.

The first term of the integrand describes the probing current from the ES to the right lead. The second term is back transport from the drain to the GS, and gives a minor correction in the forward bias condition. At the end of the high-voltage pulse at $t = t_\mathrm{h}$, an electron can remain in the ES and GS with the probabilities $\rho_\mathrm{e}(t_\mathrm{h})$ and $\rho_\mathrm{g}(t_\mathrm{h})$, respectively. When the gate voltage is switched back to V_l, the residual transport is described by the rate equations

$$\begin{aligned}\frac{\mathrm{d}}{\mathrm{d}t}\rho_\mathrm{e} &= -(\Gamma_{\mathrm{L,e}} + \Gamma_{\mathrm{R,e}} + W)\rho_\mathrm{e},\\ \frac{\mathrm{d}}{\mathrm{d}t}\rho_\mathrm{g} &= -(\Gamma_{\mathrm{L,g}} + \Gamma_{\mathrm{R,g}})\rho_\mathrm{g} + W\rho_\mathrm{e},\end{aligned} \tag{7}$$

with the initial conditions $\rho_\mathrm{e}(t_\mathrm{h})$ and $\rho_\mathrm{g}(t_\mathrm{h})$. The average number of tunnelling electrons, $\langle n_\mathrm{l}\rangle$, in a sufficiently long period of the low-voltage state, t_l (this can be replaced by infinity in the condition assumed), is given by

$$\langle n_\mathrm{l}\rangle = \int_{t=t_\mathrm{h}}^{\infty} [\Gamma_{\mathrm{R,e}}\rho_\mathrm{e} + \Gamma_{\mathrm{R,g}}\rho_\mathrm{g}]\,\mathrm{d}t. \tag{8}$$

Therefore, the total number of tunnelling electrons per pulse is obtained from

$$\langle n(t_\mathrm{h})\rangle = \langle n_\mathrm{h}\rangle + \langle n_\mathrm{l}\rangle. \tag{9}$$

Although the analytical expression for equation (9) contains different exponential terms, all curves can be approximated well by a single-exponential curve in the time domain of interest. Figure 3(a) shows the variation of $\langle n(t_\mathrm{h})\rangle$ for various relaxation rates, $W = 10^3$–10^7 Hz, under the conditions $\Gamma_{\mathrm{L,e}} = \Gamma_{\mathrm{L,g}} = 10^9$ Hz and $\Gamma_{\mathrm{R,e}} = \Gamma_{\mathrm{R,g}} = 10^6$ Hz. We made numerical calculations for equation (9), and approximated it as a single-exponential function:

$$\langle n(t_\mathrm{h})\rangle \simeq n_\mathrm{max}[1 - \exp(-Dt_\mathrm{h})]. \tag{10}$$

Here, n_max is the maximum number of tunnelling electrons that can be obtained with a sufficiently long t_h, and D is the decay rate that describes the transient transport. D is determined so as to satisfy $\langle n(1/D)\rangle = n_\mathrm{max}(1 - 1/\mathrm{e})$. n_max and D are plotted as solid curves in figures 3(b) and (c) respectively for forward bias.

Similar calculations were done for the reverse bias condition, where an electron is injected from the thicker barrier with the slow rate Γ_R and is ejected from the thinner barrier with the

fast rate Γ_L (dashed lines in figures 3(b) and (c)). In this case, an electron easily enters the GS, and immediately ceases showing transient transport.

As clearly seen from the figures, D and n_{max} for reverse bias are independent of W, while those for forward bias depend strongly on W. Therefore, one can determine the tunnelling rates from the reverse bias condition. D for reverse bias, D_{rev}, gives the total tunnelling rate $D_{rev} \sim \Gamma_{tot,g} = \Gamma_{L,g} + \Gamma_{R,g} \sim \Gamma_{L,g}$. Small $n_{max,rev}$ reflects the asymmetry of the tunnelling rates, $\sim\Gamma_R/\Gamma_L$. Combining this with the conventional dc tunnelling current, $e\Gamma_{R,g}$, through just the GS, $\Gamma_{L,e}$ and $\Gamma_{R,e}$ can be estimated separately. It should be noted for the later discussion that the total *incoming* rate, from both barriers, governs D_{rev}.

In contrast, D_{for} for forward bias can vary from Γ_R to Γ_L, and $n_{max,for}$ can vary from $\sim$1 to Γ_R/Γ_L depending on W. Therefore, the decay rate D in forward bias gives the relaxation rate W, provided that

$$\Gamma_L \gtrsim W \gtrsim \Gamma_R. \tag{11}$$

This condition can also be realized experimentally if $n_{max,for}$ for forward bias is smaller than $\sim$1 but larger than $n_{max,rev}$, or if D_{for} is smaller than D_{rev} but larger than Γ_R.

Another useful measurement for determining the tunnelling rates can be performed by changing t_l with a sufficiently long t_h. The bias polarity can be either forward or reverse in principle, but forward bias is preferred for a higher current. Under the condition $t_h \gg \Gamma_R^{-1}$ at $V_g = V_h$, the QD ends up in the N_0-electron GS after the pulse, i.e., $\rho_e(t_h) = 0$ and $\rho_g(t_h) = 1$. During the next low-voltage pulse, an electron in the GS leaves the QD at a rate given by $\Gamma_{tot,g} = \Gamma_{L,g} + \Gamma_{R,g}$. Since this extraction is required to see the transient current, the average number of tunnelling electrons is simply given by

$$\langle n(t_l)\rangle = n_{max}[1 - \exp(-\Gamma_{tot,g}t_l)], \tag{12}$$

and $\Gamma_{tot,g}$ can be obtained from the dependence on t_l. In this scheme, the total *outgoing* rate from both barriers is important.

The incoming and outgoing rates should be identical in general for tunnelling transitions between single states, but may be different if the states are degenerate. For all of the measurements presented in this article, Zeeman splitting is unresolved, and spin degeneracy effectively remains even in a magnetic field ($B < 10$ T). In this case, there are multiple tunnelling paths from the (N_0-1)-electron state to N_0-electron state. For a tunnelling transition between a state with total spin S_0 and another state with spin S_1, the ratio of incoming and outgoing rates is given by $(2S_0 + 1)/(2S_1 + 1)$, which should be between 0.5 and 2 since $S_1 = S_0 \pm 1/2$ [17]. This multi-level effect is not taken into account in the above discussions and following analysis. Although we do find that the incoming rate and the outgoing rate are different, we could not separate this effect from other effects, such as voltage dependent tunnelling rates [18].

2.3. Double-step pulse measurement

An improved method for determining the longer relaxation time, i.e., $W < \Gamma_{R,e}$, involves the application of a double-step voltage pulse, in which V_g is switched between three voltages, V_l, V_h, and V_m, as shown in figure 4(a) [16]. As compared to the single-step pulse scheme, pumping and probing sequences are now clearly separated in this scheme. Initially, when $V_g = V_l$ (figure 4(b)), empty N_0 states are prepared during a sufficiently long period of time, t_l. When V_g is suddenly increased to V_h (figure 4(c)) such that both the N_0-electron ES and GS are located below the chemical potentials, an electron enters either the ES or the GS. Once an electron enters either of these two states, it cannot leave the dot, and nor can another electron enter it (CB). Effectively the QD is now isolated from the electrodes. If an electron has entered

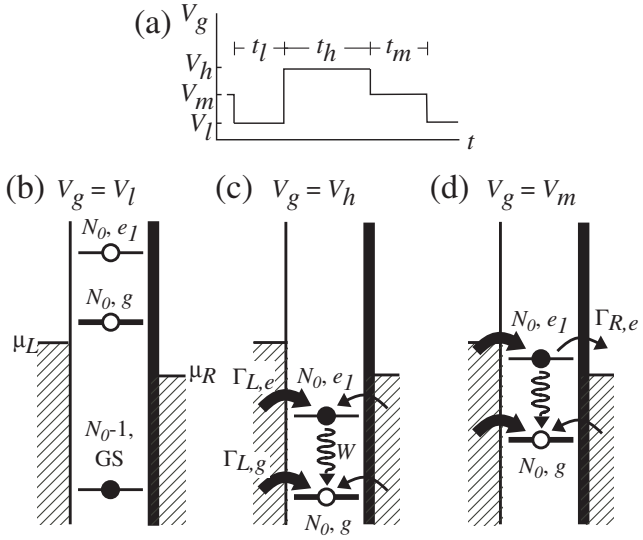

Figure 4. (a) The schematic pulse waveform for the double-step pulse measurement. (b), (c), (d) Schematic energy diagrams for the low-, high-, and medium-voltage states respectively.

the ES, the ES may relax to the GS in this high-gate-voltage state. Therefore, the average electron number in the ES after period t_h is approximately given by

$$\rho_{e,h} = A \exp(-W t_h)$$

for $t_h \gg \Gamma_L^{-1}$, where $A \simeq \frac{\Gamma_{L,e}}{\Gamma_{L,e}+\Gamma_{L,g}}$. When V_g is switched to V_m (figure 4(d)), an electron in the ES can tunnel out to the drain, if the ES has not yet relaxed to the GS. This tunnelling process can be described by equation (5) with the initial conditions $\rho_e = \rho_{e,h}$ and $\rho_g = 1 - \rho_{e,h}$. After a sufficiently long time, $t_m \gg \Gamma_{R,e}^{-1}$, for complete read-out, the average number of tunnelling electrons, $\langle n \rangle$, can be written as

$$\langle n(t_h) \rangle = A' \exp(-W t_h), \tag{13}$$

where $A' = \Gamma_{R,e}/\Gamma_{R,g}$. Therefore, the relaxation rate can be obtained from $\langle n(t_h) \rangle$. In this scheme, an electron can be pumped into the ES on the rising edge of the pulse to V_h, and then this electron can be probed while the voltage is intermediate, V_m. The N_0-electron QD may experience relaxation between the pumping and probing sequences.

We also solved a series of rate equations that describe the transport for each voltage period, and numerically obtained $\langle n(t_h) \rangle$. Figure 5(a) shows a simulation of $\langle n(t_h) \rangle$ for the double-step pulse measurement with $\Gamma_{L,e} = \Gamma_{L,g} = 10^9$ Hz and $\Gamma_{R,e} = \Gamma_{R,g} = 10^6$ Hz. $\langle n(t_h) \rangle$ can be approximated by a simple exponential curve $\langle n(t_h) \rangle = n_{max} e^{-D t_h}$, whose parameters n_{max} and D are plotted in figures 5(b) and (c). Although the signal amplitude n_{max} is different for a different bias polarity, the decay rate D is the same for both polarities. As clearly seen in figure 5(c), D directly gives the relaxation rate W over a wide range for the condition $W \ll \Gamma_L$.

3. Transient current spectroscopy

In this section, we describe the experimental procedure for single-pulse measurements and compare them with conventional dc measurements. This technique provides a spectroscopic tool which is selective as regards the relaxation time.

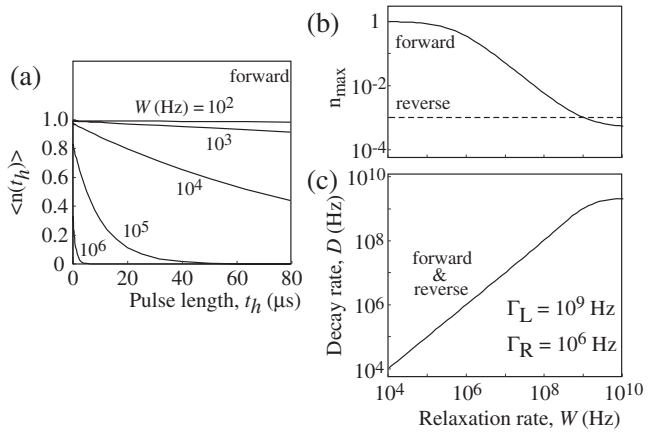

Figure 5. (a) The average number of tunnelling electrons, $\langle n(t_{\rm h})\rangle$, calculated for the double-step pulse scheme. Each curve is approximated by a single-exponential curve, whose parameters $n_{\rm max}$ and D are plotted in (b) and (c) respectively.

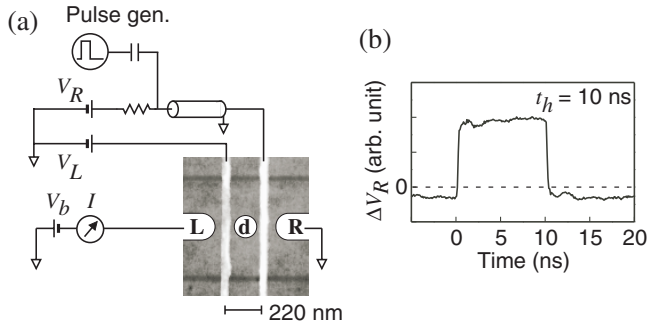

Figure 6. (a) The schematic measurement set-up for a lateral QD whose SEM image is shown. (b) The typical pulse waveform reflected back from the sample.

3.1. Lateral quantum dot

The lateral QD studied here is fabricated from an AlGaAs/GaAs modulation doped heterostructure by using focused ion beam implantation (dark horizontal lines) and Schottky gates (bright vertical lines separated by 220 nm) in the SEM (scanning electron micrograph) picture in figure 6(a). We performed all the measurements at a temperature of 150 mK and in a magnetic field applied perpendicular to the substrate [19]. The QD contains about $N \sim 50$ electrons. The charging energy is about 2 meV and the single-particle energy spacing is $\sim$100–300 μeV. We tune the two gate voltages, $V_{\rm L}$ and $V_{\rm R}$, such that the rate of tunnelling through the left barrier, $\Gamma_{\rm L}$, is much larger than that through the right barrier, $\Gamma_{\rm R}$. Figure 7(a) shows the typical current through the dot at various source–drain bias voltages $V_{\rm b}$. For negative $V_{\rm b}$ (reverse bias as defined in section 2), the current increases stepwise when a discrete state with energy E_i enters the transport window (between the left and right chemical potential, $\mu_{\rm L}$ and $\mu_{\rm R}$, respectively). $E_{\rm g}$, $E_{\rm e_1}$, and $E_{\rm e_2}$ are the energies of the GS, g, the first ES, $\rm e_1$, and the second ES, $\rm e_2$, respectively. On the other hand, for positive $V_{\rm b}$ (forward bias), current steps appear only for specific ESs; a step is seen at $\mu_{\rm L} = E_{\rm e_1}$ but apparently not at $\mu_{\rm L} = E_{\rm e_2}$ in

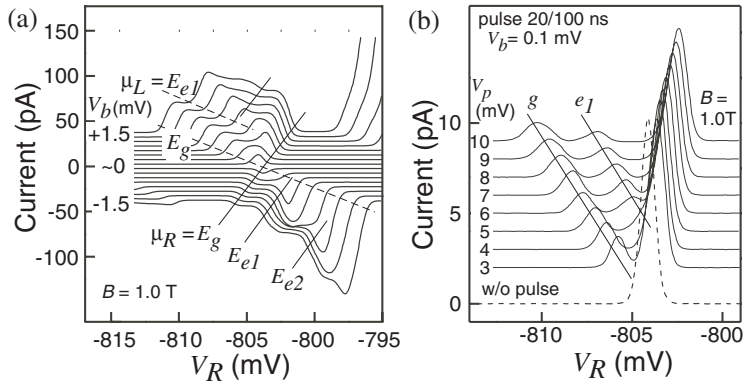

Figure 7. (a) The dc spectrum for forward (upper traces) and reverse (lower traces) bias. Each trace is offset for clarity. (b) The pulse excited current spectrum for forward bias condition ($V_b = 0.1$ mV).

figure 7(a). According to the discussion in section 2.1, this implies that the first ES must have a long relaxation time, while the second ES relaxes to the first ES or GS quickly.

For the pulse measurements, we apply a rectangular pulse to the right gate of the sample to modulate the potential of the QD (figure 6(a)). In this case the pulse also changes the tunnelling rate (Γ_R), and gives rise to excess pumping current. This excess current is smaller than 10% of the signal current in the following experiments, and can be neglected. The pulse signal is combined with the dc gate voltage via a dc block (a pass band of 700 Hz–26 GHz for the pulse), and the combined signal is fed through a low-loss coaxial cable, which consists of a silver-plated stainless-steel cable from 300 to 4 K, a superconducting niobium cable from 4 K to ∼150 mK (the mixing chamber), and a copper cable from the mixing chamber to the sample. There are no attenuators and no termination in the cryostat. The pulse introduced from the 300 K port is transmitted to the sample, and is then reflected back to the 300 K port. The reflected pulse is monitored during the measurement by an oscilloscope. A typical reflected pulse is shown in figure 6(b). This pulse is distorted by the forward and back transmission through the cables, but it is more or less the actual pulse waveform at the gate electrode. The rise time (about 0.2 ns in this case) of the pulse is shorter than $\Gamma_{L,g}^{-1}$ (about 1 ns). The rectangular waveform contains a small ringing structure and fluctuations (<10% of the pulse height in the experiment), which slightly broadens the current peak and degrades the energy selectivity.

In practice, we always sweep the dc gate voltage V_R and keep the pulse height constant; i.e., V_h and V_l are swept simultaneously. Figure 7(b) shows the pulse excited current measured at a small forward bias voltage ($V_b = 0.1$ mV). The application of the pulse signal splits the purely dc peak into two peaks. These correspond to the tunnelling through the GS in the high-voltage state (labelled g in the figure) and the low-voltage state (the rightmost peak). An extra peak (labelled e_1), which is the transient current through the first ES, appears between the two split peaks. This peak appears only when the first ES is located in the transport window in the low-voltage state. The peak spacing between g and e_1 is independent of the pulse amplitude, and the corresponding energy spacing agrees well with that obtained from normal dc measurements.

We investigate these current peaks as a function of the high-voltage pulse length, t_h. We can obtain the average number of tunnelling electrons per pulse, $\langle n_g \rangle$, for the stable current through the GS, and $\langle n_e \rangle$ for the transient current through the first ES from the $I\,(t_h + t_l)/e$ value for each peak current, I. Figures 8(a) and (b) show $\langle n_g \rangle$ and $\langle n_e \rangle$ measured at slightly different

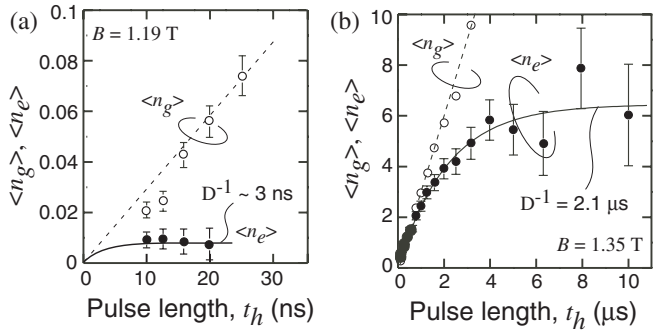

Figure 8. The average number of tunnelling electrons, $\langle n_{\rm g}\rangle$ for the stable SET current through the GS and $\langle n_{\rm e}\rangle$ for transient current through a first ES measured (a) at $B = 1.19$ T and (b) at $B = 1.35$ T.

magnetic fields ($B = 1.19$ T for (a) and 1.35 T for (b)). From the B dependence of the excitation spectrum (described below), the ESs show complicated crossing and anti-crossing behaviour at around $B = 1.3$ T, while the characteristic of the GS is unchanged for $B = 1.1$–1.5 T. The transient currents observed in figures 8(a) and (b) originate from ESs with different quantum numbers. For both cases, $\langle n_{\rm g}\rangle$ depends linearly on $t_{\rm h}$, indicating a continuous current flow. The slopes of these traces, $\mathrm{d}\langle n_{\rm g}\rangle/\mathrm{d}t_{\rm h} = \Gamma_{\rm R,g} \sim (300\ \mathrm{ns})^{-1}$, are almost the same for the two cases. For the transient current, $\langle n_{\rm e}\rangle$ shows saturation behaviour, which appears at very different pulse lengths, $t_{\rm h}$. From fitting with a single-exponential function, $\sim(1 - \mathrm{e}^{-Dt_{\rm h}})$, we obtain the decay time $D^{-1} = 2.1\ \mu$s for $B = 1.35$ T. A clear exponential curve is not obtained for $B = 1.19$ T, but the saturated value of $\langle n_{\rm e}\rangle$ for $t_{\rm h} = 10$–20 ns indicates $D^{-1} \lesssim 2$ ns.

In order to obtain the relaxation rate W from D, the condition given by equation (11) has to be confirmed. However, the condition is not safely satisfied for all the measurements performed on this sample. For $B = 1.35$ T, $D = (2.1\ \mu\mathrm{s})^{-1} = 0.5$ MHz is smaller than $\Gamma_{\rm R,e} \sim 4.2$ MHz, implying that D is not determined by W but instead probably by the tunnelling rates. We can only say that the relaxation time is comparable to or longer than 2 μs for this case. As for $B = 1.19$ T, $D \gtrsim (2\ \mathrm{ns})^{-1} = 0.5$ GHz is close to the other tunnelling rate $\Gamma_{\rm L} \sim 1$ GHz. Thus the relaxation time is comparable to or shorter than 2 ns for this particular case.

The significant difference (more than three orders of magnitudes) between the relaxation times can be qualitatively understood in terms of spin conservation during relaxation. If the ES and GS have the same spin, the ES quickly relaxes to the GS as a result of fast electron–phonon interaction (typically about $\tau_{\rm e-ph} \sim 1$ ns) [20]. In contrast, if the ES and GS have different spins, the relaxation time is limited by spin-flip processes. Most of the spin relaxation mechanisms discussed for 3D or 2D electrons in GaAs are suppressed for the 0D states of QDs. We expect an extremely long spin relaxation time ($\tau_{\rm spin} > 10\ \mu$s) due to the small spin–orbit interaction [21]. This is beyond the experimental limit (a few microseconds) of our single-pulse scheme. Therefore, the long-lived ES can have a different spin from the GS. In our experiment, the Zeeman splitting is unresolved. Thus the difference in total spin is responsible for the long energy relaxation time, and for the appearance of the transient current.

The relaxation time cannot be determined in practice, yet the single-pulse excitation scheme is useful to analyse the spin states in a spectroscopic way. On application of a square pulse ($t_{\rm h} = t_{\rm l}$), the amplitude of the net transient current, $I_{\rm e}$, is approximately given by

$$I_{\rm e} = \langle n_{\rm e}\rangle e/(t_{\rm h} + t_{\rm l}) \sim \tfrac{1}{2} eA\Gamma_{\rm R,e}/Dt_{\rm h}(1 - \mathrm{e}^{-Dt_{\rm h}}). \tag{14}$$

The transient current $I_{\rm e}$ for the two cases of $B = 1.19$ and 1.35 T can be well fitted with

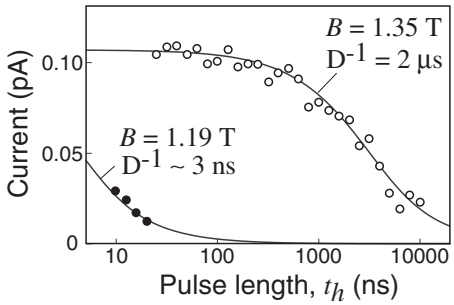

Figure 9. The peak current of the transient current measured at $B = 1.19$ and 1.35 T for various pulse lengths.

equation (14), as shown in figure 9. With an appropriate value of t_h close to Γ_R^{-1}, the transient current appears only for an ES whose total spin is different from those of all lower-lying states. This technique is useful for spectroscopic studies in a magnetic field.

The magnetic field dependences of the conventional dc and the pulse excited transient current are compared for two consecutive SET current stripes, n_0 and $n_0 + 1$, in figure 10. In the derivative of the conventional dc, dI/dV_R, for reverse bias $V_b = -1$ mV (figure 10(a)), a peak appears when any ground or ES enters the transport window. The peak positions are shown by solid curves in (d). The orbital characteristics of the states are reflected by the dependences of B on the position (energy) and the current amplitude of the peaks [3]. The complicated B dependence is a result of crossing or anti-crossing between different energy states in the dot.

In contrast, only long-lived ESs and GSs should appear in the pulse excited current spectrum measured with $V_p = 10$ mV: $t_h = 20$ ns and $t_l = 80$ ns (figure 10(c)). This spectrum is qualitatively identical to the dc spectrum in forward bias (figure 10(b)), although the pulse excited current is somewhat broadened because of the pulse waveform. The pulse length dependence on the transient current indicates that all the peaks which appear in (c) have a relaxation time longer than the corresponding tunnelling time. These long-lived ESs are also marked by hatches in (d). Other short-lived ESs are not present in figures 10(b) and (c).

Between 1 and 2 T, where edge states are developing, some states (peaks α, β, and γ for the n_0 stripe, and β', γ' and δ' for the $n_0 + 1$ stripe) decrease energetically with increasing B. They can be assigned to states in the lowest Landau level with different angular momentum. Some of the ESs (β and γ') have an extremely long relaxation time, even though these states are spatially overlapped with the GS. A long relaxation time has been reported when the states are spatially separated or the two states are attributed to different edge states [22, 23], but this is not the case here.

Some ESs (e.g., the first ES peak ξ of the n_0 stripe between 0.2 and 0.6 T) are parallel to the GS (peak ζ). The parallel GS and ES in the pair are likely to have the same orbital character but a different spin configuration due to exchange interactions. These parallel pairs actually appear in the pulse excited current demonstrating that the relaxation between the states is long. This behaviour supports our spin conservation model in the relaxation process.

However, there are some features that we still do not understand [14]. For instance, peak β (see figure 10(d)) appears as a long-lived ES only for $B > 1.25$ T. Peak β appears to cross (or anti-cross) with peak ε. Note that the transient currents in figures 8 and 9 are taken for peak ε ($W^{-1} \lesssim 2$ ns) at $B = 1.19$ T and peak β ($W^{-1} \gtrsim 2$ μs) at $B = 1.35$ T. We would expect a long-lived ES on both sides of the crossing. The signal from the long-lived state might be too small to see for $B < 1.25$ T. Further measurements are required to clarify this point.

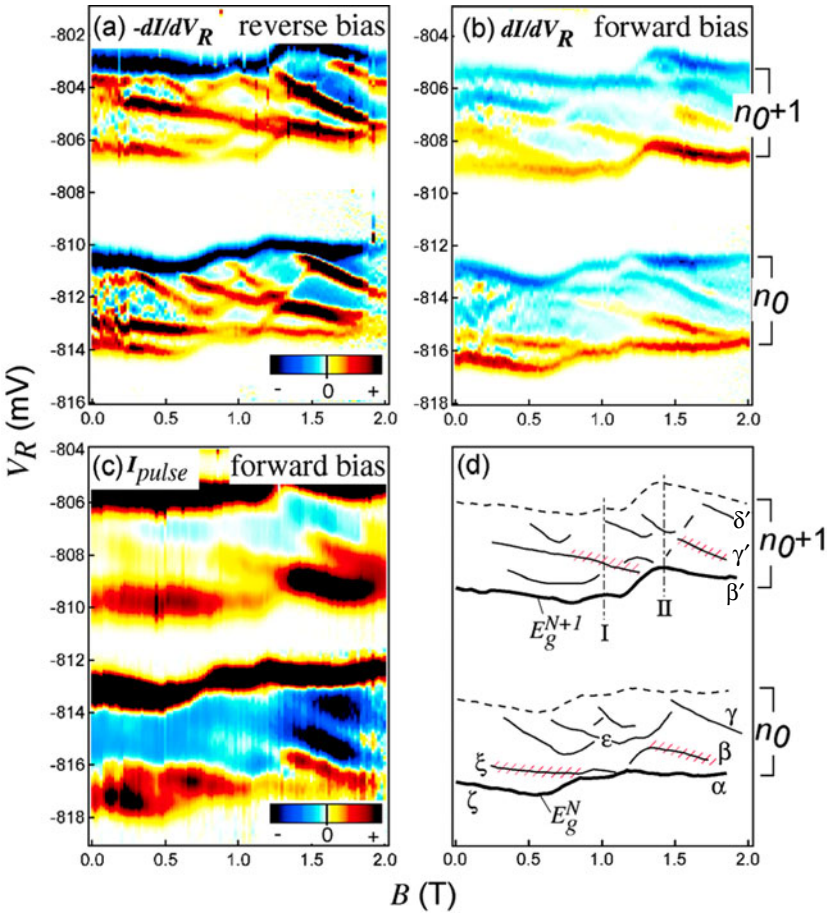

Figure 10. (a) and (b) Greyscale (colour in the electronic journal) plots of $\mathrm{d}I/\mathrm{d}V_\mathrm{R}$ from a dc transport measurement (a) for negative bias ($V_\mathrm{b} = -1$ mV) and (b) for positive bias ($V_\mathrm{b} = 1$ mV). (c) A greyscale (colour in the electronic journal) plot of the pulse excited current I measured at $V_\mathrm{b} = -0.1$ mV and $V_\mathrm{p} \sim 10$ mV. (d) Traces of the GS and ESs extracted from (a) to (c).

3.2. Few-electron vertical quantum dot

We also performed transient current spectroscopy on a vertical QD (artificial atom), in which the total number of electrons, N, and total spin, S, are well defined [4, 5, 24]. The QD is located in a circular pillar of diameter 0.5 μm fabricated from an AlGaAs/InGaAs resonant tunnelling heterostructure (see figures 11(a) and (b)). The QD is weakly coupled to the top and bottom electrodes via asymmetric $Al_{0.28}Ga_{0.72}As$ barriers (the corresponding tunnelling rate $\Gamma_\mathrm{t}^{-1} \sim 100$ ns for the 8.5 nm top barrier and $\Gamma_\mathrm{b}^{-1} \sim 3$ ns for the 7 nm bottom barrier). Electrons are confined in an $In_{0.05}Ga_{0.95}As$ quantum well (thickness $a = 12$ nm) in the vertical (z) direction, and by an approximate two-dimensional harmonic potential in lateral (x and y) directions appropriate for small N. The first few electrons occupy the 1s and 2p orbitals associated with the lateral confinement (figure 11(c)). The N dependent addition energy, $E_\mathrm{a} = 2$–5 meV, clearly reveals a shell structure for sequential electron filling just as for normal atoms. Thus, this QD is often referred to as an artificial atom. Interacting electrons inside the dot form many-body states. These states are well characterized by the total spin, S, and total

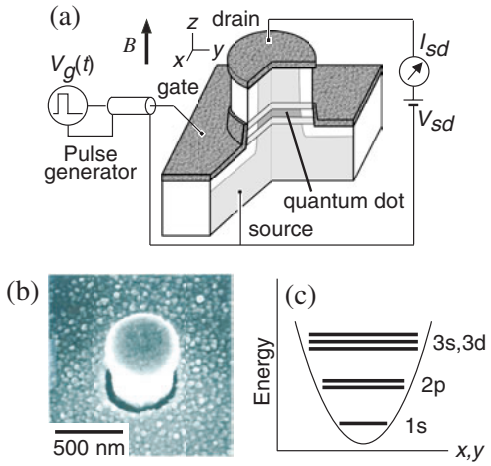

Figure 11. (a) A schematic diagram of a vertical QD with pulse measurement set-up. (b) A SEM image of a control device. (c) A schematic confinement potential of the QD.

angular momentum, M. These quantum numbers can be identified from the magnetic field (applied parallel to the current), B, dependence of the SET current spectrum. Zeeman splitting is not resolved in this measurement so we neglected it. The active region of the QD contains 5% of InAs, but we regard the dot matrix as being GaAs in the following analysis.

Figure 12(a) is the conventional dc spectrum (the grey (colour) represents the amplitude of $|\mathrm{d}I/\mathrm{d}V_\mathrm{g}|$) obtained with a reverse bias voltage $V_\mathrm{b} = -1.5$ mV. The positive peak positions within the first three stripes are traced in figure 12(c). We can identify the quantum numbers (N, S, M) of these states by comparison with an exact diagonalization calculation [25]. Inside the second stripe ($n = 2$), the ($N = 2$)-electron energy spectrum appears. We see a transition from the spin singlet state $(N, S, M) = (2, 0, 0)$, in which two anti-parallel spin electrons occupy the 1s orbital, to the spin triplet state $(N, S, M) = (2, 1, 1)$, in which two same-spin electrons occupy 1s and 2p orbitals, at $B = B_{\mathrm{S-T}} \sim 5$ T. Similarly, (N, S, M) can be identified for higher N.

For transient current spectroscopy, a small forward dc bias voltage $V_\mathrm{b} = 0.15$ mV is applied. A square pulse is applied as schematically shown in figure 11(a). Since the QD is fabricated on a conducting GaAs substrate, the parasitic capacitance of the gate electrode (mainly from the bonding pad) degrades the rise time of the pulse to 1–3 ns. This is comparable to the transport timescale ($\Gamma_\mathrm{tot}^{-1} \equiv (\Gamma_\mathrm{b} + \Gamma_\mathrm{t})^{-1} \sim 3$ ns) of the dot, and thus the amplitude of the transient current is small. However, we still see a clear transient current signal. In the following experiment, the pulse length ($t_\mathrm{h} = t_\mathrm{l} = 300$ ns) is chosen to be much longer than the typical electron–phonon scattering time $\sim$10 ns, and is comparable to Γ_t^{-1}, but is smaller than the spin relaxation time (>100 μs), so a transient current appears only for long-lived ESs whose total spin is different from those of all lower-lying states. The B dependence of the transient current spectrum is shown in figure 12(b). The lower and upper edges of each stripe are parallel due to the stable transport through the N-electron GS. The transient current through the ESs appears inside each stripe. The singlet–triplet transition for $N = 2$ is clearly seen at $B = B_{\mathrm{S-T}}$ (indicated by an arrow for the second stripe). Transient current is observed for the triplet ES when $B < B_{\mathrm{S-T}}$, and for the singlet ES when $B > B_{\mathrm{S-T}}$, since relaxation in both cases requires a spin flip.

From the third stripe in the dc spectrum (figure 12(a)), we can see some ESs whose total spin is same as that of the GS. The ES $(N, S, M) = (3, \frac{1}{2}, -1)$ appearing in the dc spectrum

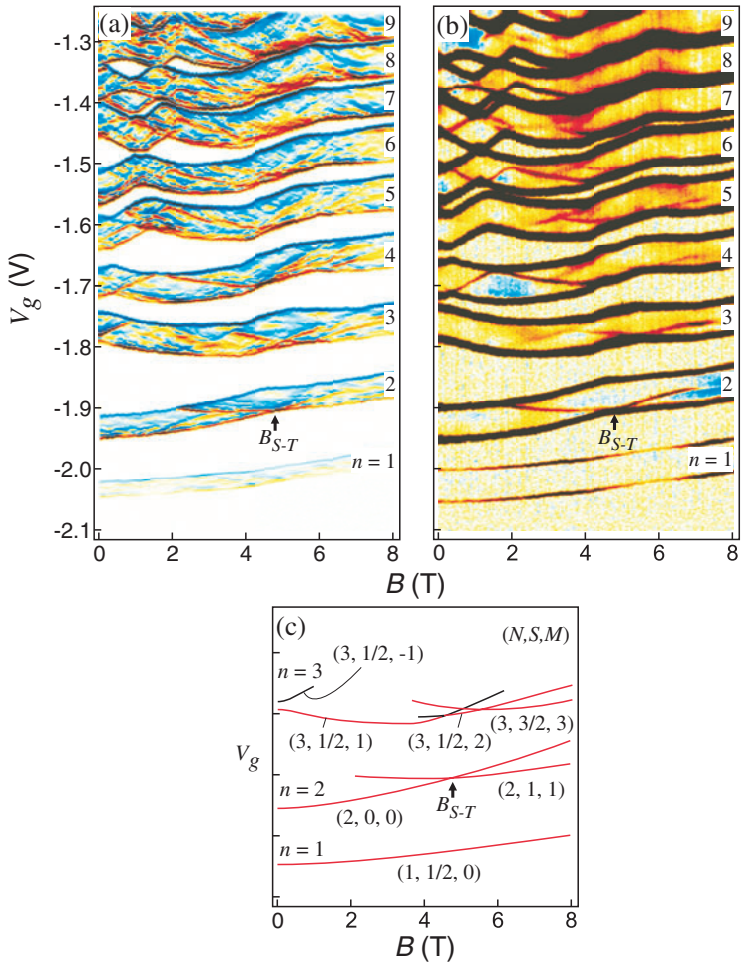

Figure 12. (a) Greyscale plots (white for zero, and grey for high) of $|\mathrm{d}I/\mathrm{d}V_\mathrm{g}|$ for reverse bias ($V_\mathrm{b} = -1.5$ mV) in a dc transport measurement. (In colour in the electronic journal, blue for negative, white for zero, red for positive.) (b) A greyscale (colour) plot of the pulse excited current I. (c) Traces of GS and ESs extracted from (a) and (b).

between 0 and 1 T can relax immediately to the GS $(3, \frac{1}{2}, 1)$ without a spin flip. Note that this ES is missing in the transient current spectrum of figure 12(b). Similarly, the ES $(3, \frac{1}{2}, 1)$ near 5 T, where it relaxes to the GS $(3, \frac{1}{2}, 2)$ without a spin flip, is also missing in the transient current. We do not see any transient current (<50 fA) for these short-lived states even when the pulse length is reduced to $t_\mathrm{h} = t_\mathrm{l} = 20$ ns. The absence of the transient signal implies that the momentum relaxation time is shorter than ∼10 ns.

One can see additional differences between the dc and pulse current spectra. The dc spectrum has many extra weak features, which do not show any clear B dependence. These fluctuations probably originate from weak modulation of the density of states in the top electrode, since its volume is relatively small ($\sim(0.5\ \mu\mathrm{m})^3$) [5, 7]. These features are suppressed in the transient current spectrum, since transport is allowed only when an ES is located in the narrow transport window. However, we see weak modulation in the amplitude of the transient current, although this is not clear from the scale used in figure 12(b).

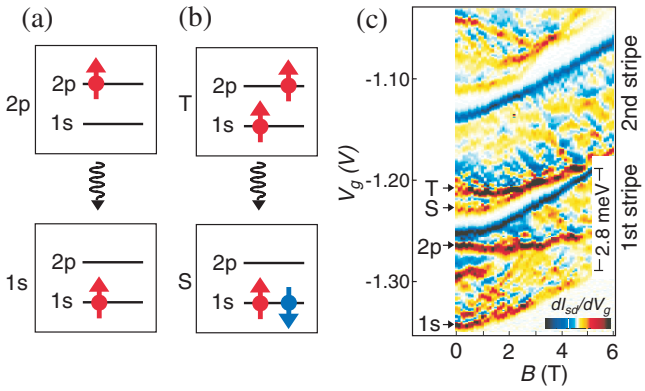

Figure 13. (a) The process of momentum relaxation from the 2p state to 1s state in the $N = 1$ QD. (b) The process of spin relaxation from the triplet state (T) to the singlet state (S) in the $N = 2$ QD. (c) Greyscale (colour) plots of $\mathrm{d}I/\mathrm{d}V_\mathrm{g}$ for negative bias ($V_\mathrm{b} = -2.8$ mV).

4. Momentum relaxation process

In this section, we investigate the momentum relaxation process in the $N = 1$ vertical QD, which is the simplest case to study. This QD can be regarded as an artificial hydrogen atom, since it has just one electron in the system. The electron occupies the 1s orbital (the GS) or the 2p orbital (the first ES). We consider the simplest process of relaxation from the 2p state to the 1s state. This transition changes the electron's orbital angular momentum but preserves the spin, as shown schematically in figure 13(a) [26]. The 2p state in a circular disc QD has twofold degeneracy, which complicates the analysis. Thus a slightly non-circular (approximately elliptic) QD is helpful for lifting the orbital degeneracy of the 2p single-particle states. This non-circularity occurs in practice in all circular QD mesas [27]. Nonetheless, we still use 1s, 2p, ... to label the orbitals for convenience. This non-circularity does not affect our discussion or the underlying physics much. The following experiments were carried out at a temperature, T, of ∼100 mK, unless otherwise stated.

The energy spectrum of these states is obtained by dc transport spectroscopy as shown by the plots of $\mathrm{d}I_\mathrm{sd}/\mathrm{d}V_\mathrm{g}$ in a magnetic field in figure 13(c). The energy spacing between the 1s and 2p states, $\varepsilon_{1\mathrm{s}-2\mathrm{p}}$, for the $N = 1$ QD deduced from the first current stripe is plotted in figure 14(a). The bare lateral confinement of our QD can be approximated by two orthogonal harmonic potentials in the x–y plane [28]. The characteristic confinement energies, $\hbar\omega_x \sim 2.5$ meV and $\hbar\omega_y \sim 5.5$ meV, are obtained by fitting $\varepsilon_{1\mathrm{s}-2\mathrm{p}}$ (see the solid curve). The corresponding characteristic size of the QD in the x/y direction is given by

$$l_{x/y} = \sqrt{\hbar/m^*}(\omega_{x/y}^2 + \omega_\mathrm{c}^2/4)^{-1/4}, \tag{15}$$

where m^* is the effective mass and $\hbar\omega_\mathrm{c}$ is the cyclotron energy. The variation of the characteristic size, $l_{x/y}$, in the magnetic field is shown in figure 14(b). The Zeeman splitting of the electron spin is small ($E_\mathrm{Z} \sim 0.1$ meV at $B = 5$ T), and is unresolved in our experiments.

The single-rectangular-pulse technique is used to measure the momentum relaxation time. Figure 15 shows the typical transient current converted into $\langle n_\mathrm{for}\rangle$ in forward bias obtained for various magnetic fields, B. $\langle n_\mathrm{for}\rangle$ can be fitted well with equation (10) (see the solid curves), and the small saturation value of $\langle n_\mathrm{for}\rangle \sim 0.02 \ll 1$ indicates very efficient relaxation. The saturation value of $\langle n_\mathrm{for}\rangle$, which varies from 5×10^{-3} to 5×10^{-2}, does not always change systematically with B, probably because the rise time of the pulse is comparable to Γ_L^{-1}, and

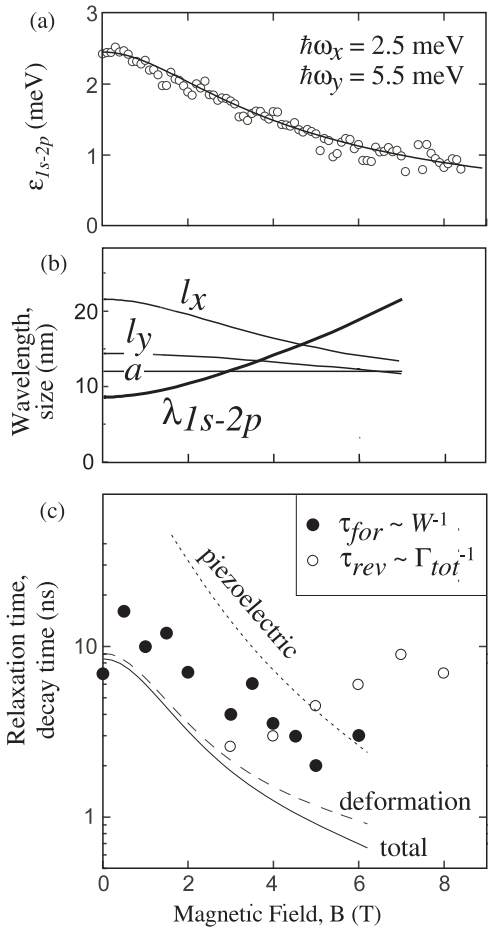

Figure 14. (a) The energy spacing, ε_{1s-2p}, between 1s and 2p states in the $N = 1$ QD. (b) The size of the QD (a, l_x, and l_y) and the phonon wavelength, λ_{1s-2p}, corresponding to the energy spacing. (c) The decay time of the transient current for forward bias (solid circles) and reverse bias (open circles), and energy relaxation times calculated from the piezoelectric potential (dotted curve), or the deformation potential (dashed curve), and both potentials (solid curve).

this fluctuates with B in this sample. However, the decay time, τ_{for}, decreases systematically with increasing B, as indicated by the solid circles in figure 14(c), although there is a scatter by a factor of 2 to 3. For reference, we also measured the transient current in the reverse bias. The decay time, τ_{rev}, is plotted as open circles in figure 14(c). As explained in section 2.2, the decay rate for reverse bias should give the total tunnelling rate. We see that $\tau_{\text{rev}} \sim \Gamma_{\text{tot}}^{-1}$ increases slightly with B. This dependence is consistent with the B dependence of the conventional dc tunnelling current amplitude. For $B < 4$ T ($\tau_{\text{rev}} < \tau_{\text{for}}$), equation (11) is satisfied, and τ_{for} gives the time W^{-1} for relaxation from the ES to the GS. The momentum relaxation time is 3–10 ns, and decreases with increasing B.

Now we discuss the relaxation mechanism. For an energy spacing in the millielectronvolt region, and at low temperature (thermal energy: $\sim$10 μeV $\ll \varepsilon_{1s-2p}$), spontaneous emission of a *phonon*, rather than a photon, dominates the relaxation process [22]. The energy spacing coincides with the acoustic phonon energy in the linear dispersion regime. Because of the

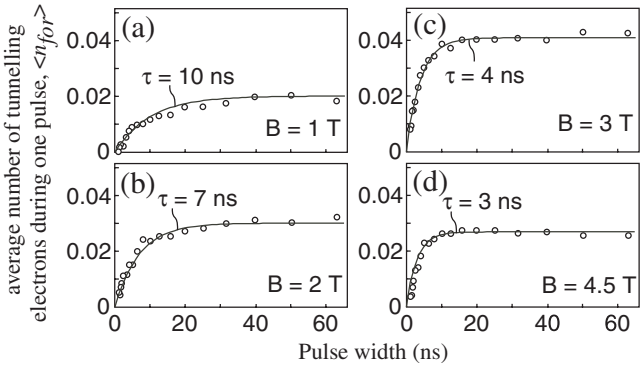

Figure 15. The average number of tunnelling electrons during one pulse, $\langle n_{\rm for}\rangle$, in the forward bias condition for different magnetic fields.

discrete energy states, the relaxation involves an emission of a phonon whose energy is identical to ε_{1s-2p}. The corresponding phonon wavelength is given by $\lambda_{1s-2p} = h v_{\rm phonon}/\varepsilon_{1s-2p}$, where $v_{\rm phonon} = 5100\ {\rm m\ s^{-1}}$ is the phonon velocity in GaAs. λ_{1s-2p}, which is plotted as a function of B in figure 14(b), is comparable to or even smaller than the size of the QD. Theoretically, the strength of the electron–phonon interaction is expected to be suppressed for phonon wavelengths smaller than the characteristic size of the QD [20]. Actually, the observed B dependence of the relaxation time can be understood since phonon emission is suppressed when λ_{1s-2p} becomes smaller than the dot size.

This suppression has been discussed in the context of inefficient optical transitions (the phonon bottleneck effect) [29–31]. However, most optical characteristics do not agree with this theory, probably because of interactions with the optical phonon, or because of the Auger mechanism [32]. Our experiments on a simple one-electron QD qualitatively indicate the signature of the phonon bottleneck effect, and reveal intrinsic phonon emission characteristics for moderate acoustic phonon energies.

In order to be more quantitative, we calculate the phonon emission rate from Fermi's golden rule:

$$W_{\rm e-p} = \frac{2\pi}{\hbar}|\langle\psi_{1s}|H_{\rm e-p}|\psi_{2p}\rangle|^2 \rho_{\rm phonon}\delta(\varepsilon_{1s-2p} - \hbar\omega), \tag{16}$$

where $\rho_{\rm phonon}$ is the phonon density of states, and $\hbar\omega$ is the phonon energy. The 1s and 2p wavefunctions in the QD, ψ_{1s} and ψ_{2p} respectively, are approximated by the wavefunction of a circular QD disc with the effective confinement energy of $\hbar\omega_{\rm eff} = \hbar\sqrt{\omega_x\omega_y(1+\omega_c^2/(\omega_x+\omega_y)^2)}$. This assumption may be reasonable, because Coulomb interactions in an elliptic QD just scale with $\hbar\omega_{\rm eff}$ [28]. We consider both deformation and piezoelectric types of coupling for the electron–phonon interaction Hamiltonian:

$$H_{\rm def} = \left(\frac{\hbar}{2\rho_{\rm GaAs}\omega}\right)^{1/2} k E_{\rm def}\exp(-{\rm i}kr), \tag{17}$$

$$H_{\rm piezo} = \left(\frac{\hbar}{2\rho_{\rm GaAs}\omega}\right)^{1/2} \frac{eE_{\rm p}}{\varepsilon^*}\exp(-{\rm i}kr), \tag{18}$$

where $\rho_{\rm GaAs}$ is the material density, $k = \hbar\omega/v_{\rm phonon}$ is the phonon wavevector, $E_{\rm def} = 8.6$ eV is the deformation potential, and $E_{\rm p} = 0.16\ {\rm C\ m^{-2}}$ is the piezoelectric constant [20, 33, 34]. Note that the ratio of the phonon emission rate for piezoelectric-type coupling, $W_{\rm piezo}$, to that

for deformation-type coupling, $W_{\rm def}$, is given by

$$\frac{W_{\rm piezo}}{W_{\rm def}} = \left(\frac{eE_{\rm p}}{\varepsilon^* k E_{\rm def}}\right)^2, \tag{19}$$

indicating that the piezoelectric effect is dominant for a phonon energy smaller than ∼0.6 meV.

The calculated relaxation times without any fitting parameter are plotted in figure 14(c). In the region of interest to us, the deformation potential coupling provides the main contribution, and the total phonon emission rate (solid curve) agrees well with experiment. The difference by about a factor of 2 or 3 might come from the assumptions about the confinement potential, and uncertainty in the material parameters. Thus, the fast energy relaxation in the $N = 1$ QD (artificial hydrogen atom) can clearly be understood on the basis of spontaneous emission of a phonon.

It should be noted that no clear selection rule for orbital momentum is expected for QDs. If the confinement potential is a perfect 2D symmetric harmonic potential, the selection rule for the dipole approximation, in which the phonon wavelength is much longer than the dot size, is that the difference in angular momentum quantum number is one. All orbital states (n, l), where n and l are the radial and angular momentum quantum numbers, can relax to $(n, l-1)$ by phonon emission, and eventually cascade down to the lowest $(n, 0)$ state. $(n, 0)$ states, 3s state for example, may be quasi-stable state in this approximation. However, the confinement potential of practical QDs is not completely symmetric and parabolic, and the dipole approximation cannot be applied. Therefore, a clear selection rule for phonon emission is not expected.

5. Spin relaxation processes

Compared with that for the $N = 1$ QD, the relaxation time is remarkably different for a $N = 2$ QD, which can be considered as an artificial helium atom. At low magnetic fields, the many-body GS is a spin singlet (labelled S), while the first ES is a spin triplet (labelled T) [4]. Figure 13(b) shows schematically the electron configurations of these states. Because of direct and exchange Coulomb interactions, the energy spacing between the two states, $\varepsilon_{\rm S-T}$ (∼0.6 meV at $B = 0$ T), is smaller than the energy spacing $\varepsilon_{\rm 1s-2p}$ for the $N = 1$ QD. The energy relaxation from the first ES (T) to the GS (S) for the $N = 2$ QD not only involves the same change in orbital angular momentum as that in the $N = 1$ QD, but also requires a spin flip because of Pauli exclusion. A simple phonon emission transition from the spin triplet to the spin singlet is forbidden by spin conservation.

We measure how long this inelastic spin relaxation takes. The simple rectangular pulse technique employed for the $N = 1$ QD is not useful for this $N = 2$ QD transition, because the relaxation lifetime, $\tau_{\rm S-T}$, is always beyond the measurable range ($\tau_{\rm S-T} > \Gamma_{\rm d}^{-1} \sim 100$ ns). Instead, we subject the QD to a double-step voltage pulse as introduced in section 2.3 [26]. In this case, the time dependent gate voltage $V_{\rm g}(t)$ is switched between three voltages, $V_{\rm l}$, $V_{\rm h}$, and $V_{\rm m}$, whilst the dc gate voltage is swept and the pulse height is kept constant. Each of the original SET peaks is split into three peaks, each corresponding to the three voltage states. When the pulse height exceeds a value corresponding to the energy spacing $\varepsilon_{\rm S-T}$, two transient current peaks, $e_{\rm m}$ and $e_{\rm h}$ in figure 16, appear. Peak $e_{\rm h}$ ($e_{\rm m}$) corresponds to the transient current in the high- (medium-) voltage state, and peak $e_{\rm m}$ is of particular interest. We evaluate the average number of tunnelling electrons, $\langle n_{\rm t}\rangle = I_{\rm p}(t_{\rm l} + t_{\rm h} + t_{\rm m})/e$, from the current $I_{\rm p}$ at peak $e_{\rm m}$. This measures the average number of tunnelling electrons from the unrelaxed state, $\langle n_{\rm t}\rangle = A\exp(-t_{\rm h}/\tau_{\rm S-T})$, from which we can evaluate $\tau_{\rm S-T}$. Since the relaxation time is very long, the current amplitude becomes very low, ∼1 fA, at the longest $t_{\rm h}$ of 100 μs in our

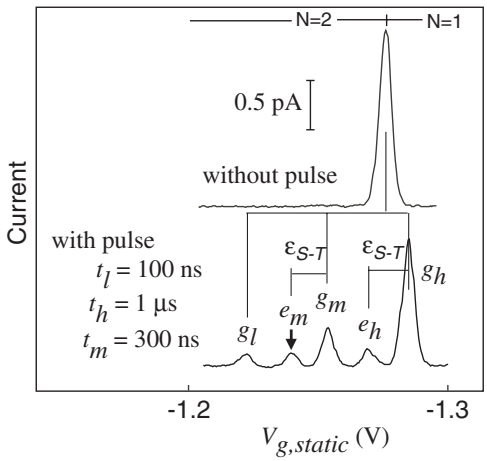

Figure 16. Typical current spectra without a pulse (upper trace) and with a double-step pulse (lower trace).

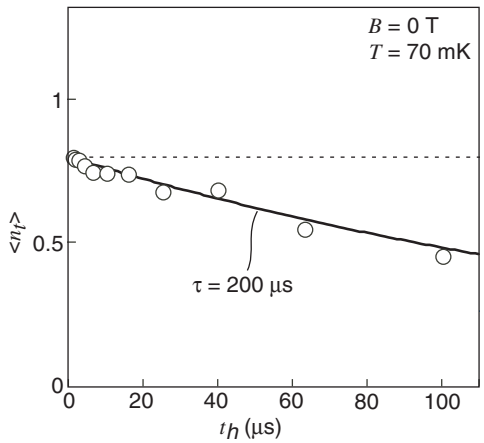

Figure 17. The average number of tunnelling electrons during a pulse, $\langle n_t \rangle$, for the triplet ES in the $N = 2$ QD.

experiment. In order to obtain a reliable current, the signal is integrated and averaged for about one hour to average out the noise of our current meter ($\sim$20 fA Hz$^{-1/2}$). Figure 17 shows a typical measurement of $\langle n_t \rangle$ at $B = 0$ T, indicating a relaxation time of $\tau_{S-T} \sim 200$ μs. This relaxation time is 4 to 5 orders of magnitude longer than that observed for the $N = 1$ QD.

5.1. Thermal excitation

First, we study thermal effects, which always enhance inelastic processes. Figure 18 shows the typical temperature dependence measured at $B = 0$ T. The relaxation time is insensitive to T up to $\sim$0.5 K, and decreases rapidly on increasing T further. Above 1.5 K, CB peaks are so broadened that we cannot safely distinguish the transient current from the stable SET current. This behaviour can be understood on the basis of thermal excitation from the triplet state to the electrodes, which then allows another electron with opposite spin to enter the QD

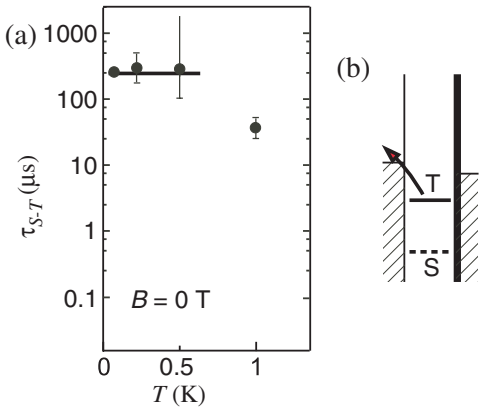

Figure 18. (a) The temperature dependence of the inelastic spin relaxation. (b) A schematic energy diagram for the thermal excitation.

and form the $N = 2$ singlet GS. This sequential tunnelling process effectively exchanges spin with the leads. Considering the Fermi–Dirac distribution, the thermally activated relaxation time is given by

$$\tau_{\rm th}^{-1} \sim \frac{1}{1+A}\Gamma_{\rm tot}/(\exp(\Delta_1/k_{\rm B}T)+1), \tag{20}$$

where Δ_1 is the energy of excitation from the triplet to the electrode. Δ_1 and $\tau_{\rm th}^{-1}$ depend on the gate voltage, and $\tau_{\rm th}$ can become short for $\Delta_1 \sim k_{\rm B}T$.

5.2. Inelastic cotunnelling effect

We find that $\tau_{\rm S-T}$ depends on the high voltage of the pulse, $V_{\rm h}$, during which relaxation takes place, as shown in figure 19(a). Although $V_{\rm h}$ is swept deep into the $N = 2$ CB region (see figure 19(b)), $\tau_{\rm S-T}$ decreases rapidly at $V_{\rm h} \sim -1.18$ V. This $V_{\rm h}$ dependence implies a strong influence of the electrodes. However, this dependence cannot be explained by the thermal excitation, since it would show a very strong $V_{\rm h}$ dependence at this temperature (indicated by dashed lines).

Even though CB is robust in the suppression of transport, higher-order tunnelling processes can contribute to the relaxation and alter $\tau_{\rm S-T}$. An electron in the dot can be exchanged with an electron of opposite spin from the electrodes. This can result in energy loss in the QD, and the electrode will gain the same energy. This inelastic cotunnelling rate, $\tau_{\rm co}^{-1}$, is estimated by considering second-order tunnelling processes [35–37]. The cotunnelling rate can be written as

$$\Gamma_{\rm T\to S}^{\alpha\to\beta} = \frac{2\pi}{\hbar}\sum_{k,k'}|T_{\rm T\to S}^{\alpha\to\beta}|^2\delta(\varepsilon_{\rm S-T}+E_{\alpha,k}-E_{\beta,k'})f(E_{\alpha,k}-\mu_\alpha)[1-f(E_{\alpha,k}-\mu_\alpha)], \tag{21}$$

in which an electron with momentum k in lead α is scattered to a state with momentum k' in the lead β during the process of inelastic spin relaxation from the triplet (T) to the singlet (S). For the relaxation mechanisms considered here, the $N = 2$ QD can relax virtually through $N = 1$ or 3 intermediate states. $T_{\rm T\to S}^{\alpha\to\beta}$ is the scattering matrix which describes these transition processes, and can be written as

$$T_{\rm T\to S}^{\alpha\to\beta} = V_\beta^* V_\alpha(\Delta_1^{-1}+\Delta_3^{-1}), \tag{22}$$

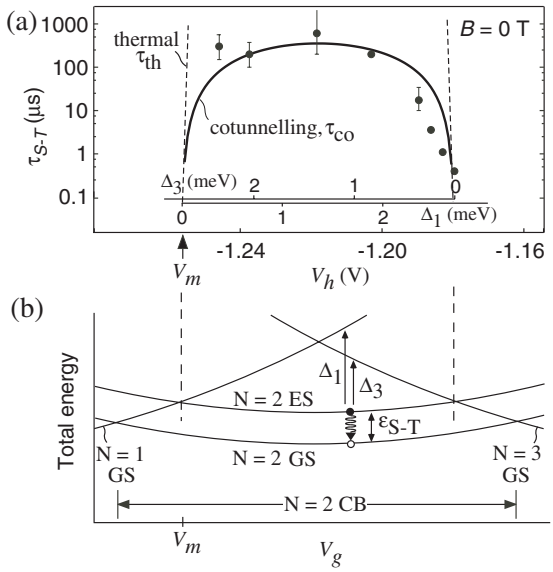

Figure 19. (a) The gate voltage dependence of the inelastic spin relaxation time. (b) The total energy diagram for inelastic spin relaxation.

where V_α and V_β are transmission amplitudes of the corresponding barrier. Δ_1 and Δ_3 are the excitation energies from the triplet state to $N = 1$ and 3 GS, respectively. We sum up all the contributions from both electrodes (α, $\beta \in \{\mathrm{L}, \mathrm{R}\}$):

$$\tau_{\mathrm{cot}}^{-1} = \Gamma_{\mathrm{T}\to\mathrm{S}}^{\mathrm{L}\to\mathrm{L}} + \Gamma_{\mathrm{T}\to\mathrm{S}}^{\mathrm{L}\to\mathrm{R}} + \Gamma_{\mathrm{T}\to\mathrm{S}}^{\mathrm{R}\to\mathrm{L}} + \Gamma_{\mathrm{T}\to\mathrm{S}}^{\mathrm{R}\to\mathrm{R}}, \tag{23}$$

and this can be simplified by assuming zero bias voltage ($\mu_{\mathrm{L}} = \mu_{\mathrm{R}}$) and zero temperature:

$$\tau_{\mathrm{cot}}^{-1} = \varepsilon_{\mathrm{S-T}}(\hbar\Gamma_{\mathrm{tot}})^2(\Delta_1^{-1} + \Delta_3^{-1})^2/h, \tag{24}$$

where $\Gamma_{\mathrm{tot}} = \Gamma_{\mathrm{L}} + \Gamma_{\mathrm{R}}$ is the total tunnelling rate. Note that this process does not cause a net current even at a finite voltage of $e|V_{\mathrm{sd}}| < \varepsilon_{\mathrm{S-T}}$ [38].

Figure 19(b) shows the total energy of the $N = 1$, 2, and 3 QD, involving the $N = 2$ ES. We can define Δ_1 and Δ_3 ($=E_{\mathrm{a}}-2\varepsilon_{\mathrm{S-T}}-\Delta_1$) from this figure, and Δ_1 and Δ_3 are also indicated in figure 19(a). The solid line in figure 19(a) shows τ_{co}, calculated from equation (24) with experimentally deduced parameters ($\varepsilon_{\mathrm{S-T}} = 0.6$ meV, and $\Gamma_{\mathrm{tot}}^{-1} = 7$ ns) but without any fitting parameter. Clearly the observed relaxation time can be well understood on the basis of an inelastic cotunnelling process. The maximum observed relaxation time of about 200 μs is determined by the cotunnelling process. Here, in order to account for the decreasing relaxation time on the more positive V_{h} side, we use $\Gamma_{\mathrm{tot}}^{-1} = 7$ ns which is obtained for the total incoming tunnelling transition from the $N = 2$ triplet state to $N = 3$ GS. However, we do not see a clear decrease of the relaxation time on the more negative V_{h} side, even through the corresponding tunnelling rate is faster. The rate of $\Gamma_{\mathrm{tot}}^{-1} = 3$ ns is obtained for the total outgoing tunnelling transition from the $N = 2$ triplet state to $N = 1$ GS. This discrepancy is not yet well understood.

We find no clear B dependence of $\tau_{\mathrm{S-T}}$ (always longer than 100 μs), at least for the energy spacing between 0.6 meV at $B = 0$ T and 0.24 meV at $B = 2$ T (figure 20). The cotunnelling rate given by equation (24) suggests a magnetic field dependence determined by $\varepsilon_{\mathrm{S-T}}$, Γ_{tot}, and $\Delta_{1/3}$. For the magnetic field region from 0 to 2 T, $\varepsilon_{\mathrm{S-T}}$ decreases by about half, and Γ_{tot} may also decrease by about half, while $\Delta_{1/3}$ does not change very much. So τ_{cot}^{-1} can increase

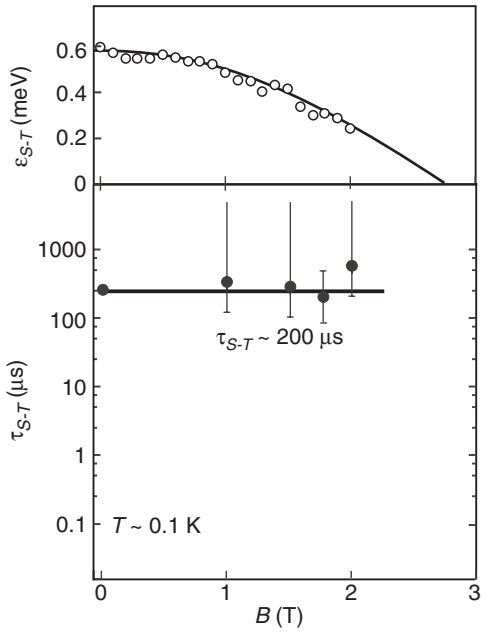

Figure 20. The magnetic field dependence of the energy spacing (upper panel) and of the inelastic spin relaxation time (lower panel).

by a factor of ∼8, which is within the error bar of our experiment. More detailed experiments will clarify this dependence.

5.3. Spin–orbit interactions

It should be noted that the cotunnelling process can be easily reduced by using even thicker tunnelling barriers. Then we would expect a much longer relaxation time, which would be dominated by intrinsic processes. Very importantly, the large difference between τ_{1s-2p} and τ_{S-T} originates from the fact that other effects, such as spin–orbit and hyperfine interactions [10, 21], must have only a weak effect on the breaking of the 'forbidden' symmetries. We now discuss how small these hidden contributions are by focusing on the spin–orbit interactions.

Spin–orbit interactions are predicted to give the dominant contribution to spin relaxation in GaAs QD systems [21], although this is still an extremely small effect. Spin–orbit interaction can originate from the absence of crystal inversion symmetry, confinement potential, and interface or surface effects. For simplicity, we consider the spin–orbit interaction energy:

$$\Delta_{so} = |\langle \psi_{1s,\uparrow/\downarrow} | H_{so} | \psi_{2p,\downarrow/\uparrow} \rangle|, \tag{25}$$

only for coupling between the 1s and 2p orbitals of opposite spin. We do not discuss the microscopic origin of the interaction Hamiltonian, H_{so}, in detail. This interaction mixes the spin up and down electron wavefunctions, which can be written as

$$\begin{aligned} \tilde{\psi}_{1s,\uparrow/\downarrow} &= \psi_{1s,\uparrow/\downarrow} - \frac{\Delta_{so}}{\varepsilon_{1s-2p}} \psi_{2p,\downarrow/\uparrow}, \\ \tilde{\psi}_{2p,\uparrow/\downarrow} &= \psi_{2p,\uparrow/\downarrow} + \frac{\Delta_{so}}{\varepsilon_{1s-2p}} \psi_{1s,\downarrow/\uparrow}. \end{aligned} \tag{26}$$

Here $\psi_{1s,\uparrow/\downarrow}$ ($\psi_{2p,\uparrow/\downarrow}$) is the unperturbed wavefunction of a spin up/down electron in the 1s (2p) orbital. The two-electron wavefunction for $N = 2$ QD can be approximated by the Slater determinant of the one-electron 1s and 2p wavefunctions, and the $N = 2$ spin singlet and triplet states in the presence of the spin–orbit interaction can be written as

$$\begin{aligned}\tilde{\psi}_{\mathrm{S}} &= \psi_{\mathrm{S}} - \frac{\Delta_{\mathrm{so}}}{\varepsilon_{\mathrm{S-T}}}\psi_{\mathrm{T},1} - \frac{\Delta_{\mathrm{so}}}{\varepsilon_{\mathrm{S-T}}}\psi_{\mathrm{T},-1},\\ \tilde{\psi}_{\mathrm{T},\pm1} &= \psi_{\mathrm{T},\pm1} + \frac{\Delta_{\mathrm{so}}}{\varepsilon_{\mathrm{S-T}}}\psi_{\mathrm{S}}.\end{aligned} \tag{27}$$

We consider the electron–phonon interaction for the transition between these states, and the corresponding transition rate can be written as

$$W_{\mathrm{so}} = \frac{2\pi}{\hbar}\left(\frac{\Delta_{\mathrm{so}}}{\varepsilon_{\mathrm{S-T}}}\right)^2 |\langle\psi_{2\mathrm{p}}|H_{\mathrm{e-p}}|\psi_{2\mathrm{p}}\rangle|^2 \rho_{\mathrm{phonon}}(\varepsilon_{\mathrm{S-T}}), \tag{28}$$

which is obtained by substituting equation (27) for (16). For a parabolic confinement potential, the matrix element can be approximated by

$$|\langle\psi_{2\mathrm{p}}|H_{\mathrm{e-p}}|\psi_{2\mathrm{p}}\rangle| \approx |\langle\psi_{1\mathrm{s}}|H_{\mathrm{e-p}}|\psi_{2\mathrm{p}}\rangle|, \tag{29}$$

and the spin–orbit relaxation rate is simplified to

$$W_{\mathrm{so}} = \left(\frac{\Delta_{\mathrm{so}}}{\varepsilon_{\mathrm{S-T}}}\right)^2 W_{\mathrm{e-p}}(\varepsilon_{\mathrm{S-T}}), \tag{30}$$

where $W_{\mathrm{e-p}}(\varepsilon_{\mathrm{S-T}})$ is the phonon emission rate at the transition energy $\varepsilon_{\mathrm{S-T}}$. We know that the momentum relaxation time can be well accounted for by the phonon emission process as discussed in section 4.

For our QD at $B = 0$ T, we speculate that $W^{-1}_{\mathrm{e-p}}(\varepsilon_{\mathrm{S-T}} = 0.6\ \mathrm{meV}) = 0.5$–3 ns, in which piezoelectric and deformation coupling contribute to the relaxation almost equally. Since the spin–orbit relaxation time should be longer than the observed cotunnelling relaxation time of 200 μs, we can deduce an upper bound of $\Delta_{\mathrm{so}} < 4\ \mu$eV. This value of Δ_{so} is close to the spin–orbit induced spin splitting energy ($\sim$2.5 μeV) observed in a GaAs two-dimensional electron gas system [39]. Spin–orbit interactions are significantly enhanced in nanoparticles, e.g. copper, probably because of impurities or interfaces [40], but our vertical semiconductor QDs are largely free of these undesirable factors.

Our experiments indicate that the spin degree of freedom in QDs is well isolated from the orbital degree of freedom. This is particularly attractive for applications to spin memories and spin qubits [41]. For a simple scheme involving just a single-electron spin in a magnetic field, spin–orbit interactions can degrade the energy relaxation time (T_1) of a spin qubit. We estimate this contribution, $T_{1,\mathrm{so}}$, using a perturbative approach:

$$T^{-1}_{1,\mathrm{so}} \sim \left(\frac{\Delta_{\mathrm{so}}}{\varepsilon_{\mathrm{Z}}}\right)^2 W_{\mathrm{e-p}}(\varepsilon_{\mathrm{Z}})$$

from equations (16) and (26). Since $\Delta_{\mathrm{so}} < 4\ \mu$eV, this yields $T_{1,\mathrm{so}} > 1$ ms for a Zeeman splitting $\varepsilon_{\mathrm{Z}} \sim 0.1$ meV and $\varepsilon_{1\mathrm{s-2p}} \sim 1.2$ meV at $B \sim 5$ T ($T_{1,\mathrm{so}} > 100\ \mu$s at $B \sim 9$ T). Recent measurements [42] concerning the process of energy relaxation between Zeeman sublevels in $N = 1$ QD indicates that $T_1 \gtrsim 50\ \mu$s, which supports our estimation. Note that the estimated $T_{1,\mathrm{so}}$ is comparable to that obtained by electron spin resonance for donor states in GaAs [43], and is much longer than the time required for typical one- and two-qubit operations [44]. Small spin–orbit interactions are also desirable with respect to the dephasing time (T_2) of a spin qubit [45]. Our results are therefore encouraging for further research in the use of the spin degree of freedom in QDs.

Table 1. Comparison of processes of relaxation from the first ES (neglecting Zeeman sublevels) to the GS in artificial atoms and real atoms. The atomic species, the transition process in the atomic representation, the mechanism for the allowed or forbidden transition, and the relaxation time with the relaxation energy are shown for each item.

	Artificial atoms (QDs)	Real atoms	
One-electron system	$N = 1$ QD 2p–1s Allowed for phonon emission $\tau = 3$–10 ns ($h\nu \sim 2$ meV)	Hydrogen (H) 2p–1s (Lyman α) Allowed for photon emission $\tau = 1.6$ ns ($h\nu = 10.2$ eV)	Potassium (K) 4p–4s Allowed for photon emission $\tau = 2.6$ ns ($h\nu = 1.61$ eV)
Two-electron system	$N = 2$ QD $(1s)(2p)\ ^3P$–$(1s)^2\ ^1S$ Forbidden by spin $\tau \sim 200\ \mu$s ($h\nu \sim 0.5$ meV)	Helium (He) $(1s)(2s)\ ^3S$–$(1s)^2\ ^1S$ Forbidden by spin and parity $\tau = 7860$ s ($h\nu = 19.8$ eV)	Calcium (Ca) $(4s)(4p)\ ^3P$–$(4s)^2\ ^1S$ Forbidden by spin $\tau = 385\ \mu$s ($h\nu = 1.89$ eV)
$\tau_{\text{forbidden}}/\tau_{\text{allowed}}$	$>3 \times 10^4$	4.5×10^{12}	1.5×10^5

5.4. Comparison with real atoms

Our observations for $N = 1$ and 2 QDs (artificial atoms) can be compared with those for real atoms [46] (see table 1). The transition from the 2p state to the 1s state in atomic hydrogen is allowed by photon emission (the Lyman α transition line), while that in artificial hydrogen is allowed by *phonon* emission. The transition time of 1.6 ns at the photon energy of 10.2 eV for atomic hydrogen happens to be of the same order of magnitude as the relaxation time of 3–10 ns at the phonon energy of 1–3 meV for the artificial hydrogen atom, although the mechanisms and energy quanta are quite different.

The transition from the spin triplet state to the spin singlet state is forbidden by conservation of total spin for artificial helium. The corresponding relaxation time for atomic helium from $(1s)(2s)\ ^3S$ to $(1s)^2\ ^1S$ is extremely long (7860 s), because it is doubly forbidden by spin and momentum selection rules (the electric dipole transition from 2s to 1s is also forbidden). The difference between the allowed and forbidden transitions leads to a difference of more than 12 orders of magnitude between the relaxation times for real hydrogen and helium atoms. Our observation of a difference of 4 to 5 orders of magnitude for our $N = 1$ and 2 artificial atoms is not as high, but is comparable to that for atomic K and Ca, which are located in the same row in the periodic table as the host atoms of Ga and As in our QD. This implies that the quality of our QD is high.

6. Non-equilibrium transport

In this section, we discuss highly non-equilibrium transport characteristics, which arise as a result of the long inelastic spin relaxation time. We have shown in the previous section that the spin-flip energy relaxation time in QDs can be extremely long ($\gtrsim$200 μs). This is much longer than the typical interval for tunnelling events ($\Gamma^{-1} = 1$–100 ns for a typical tunnelling current of $e\Gamma \sim 1$–100 pA, where Γ is the tunnelling rate), while the momentum relaxation time, $\tau_{\text{mo}} \sim 10$ ns is much shorter. Therefore, no internal transition that changes the total spin of the QD occurs within the typical transport timescale.

There is another important selection rule in transport. Since a single electron has spin $1/2$, a SET transition must change the total spin by $1/2$, and other tunnelling transitions should be forbidden. The spin blockade effect has been discussed for the suppression of the conductance or the appearance of negative differential conductance [47, 48]. However, most experimental

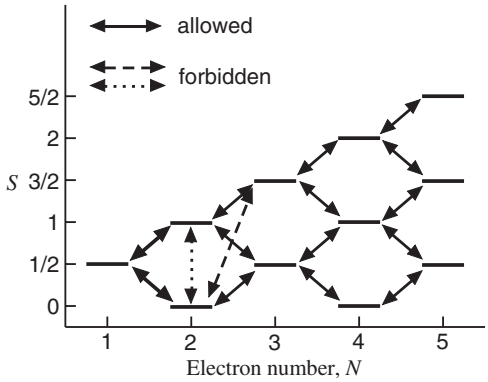

Figure 21. The possible total spin, S, for various numbers of electrons, N, in a QD. The solid arrows indicate allowed tunnelling transitions, while other transitions are forbidden.

interpretations for the weak suppression of the conductance seem to contradict the simple expectation of a complete suppression of the current.

We investigate these spin selection rules (spin conservation and the spin blockade effect) in the transport characteristics of a few-electron vertical QD. All the transport processes can be well understood on the basis of these spin selection rules. However, we find that the number of electrons, the total spin, and the total energy of the QD can fluctuate significantly due to non-equilibrium transport [49, 50].

6.1. Reconsideration of orthodox Coulomb blockade theory

Figure 21 shows the allowed and forbidden tunnelling transitions between different (N, S) states in a few-electron QD consistent with the two kinds of spin selection rule. For example, the internal transition between $(N, S) = (2, 0)$ and $(2, 1)$ (dotted arrow) is forbidden by spin conservation. The tunnelling transition between $(N, S) = (2, 0)$ and $(3, 3/2)$ (dashed arrow) is forbidden by spin blockade. These spin selection rules restrict the possible transitions in a QD, and give rise to complicated excitation processes that cannot be explained by orthodox CB theory.

The orthodox CB theory accounting for the CB effect and SET was originally introduced for transport through a small conductive island with a continuum of density of states. This theory is widely accepted for a variety of systems involving semiconductors, normal and superconducting metals, and molecules, some of which have spin dependent discrete energy states [13]. The total energy, $U(N)$, of the system, in which an island containing N electrons is electrostatically affected by a gate voltage, V_g, via a capacitance, C_g, is given by

$$U(N) = \frac{(-Ne + C_g V_g + q_0)^2}{2C_\Sigma} + E_{\text{int}}(N, S, M). \tag{31}$$

The first term is the electrostatic energy approximated by a constant Coulomb interaction. Enclosed in the parentheses is the sum of the electron charge on the dot, the charge induced by the gate, and an offset charge, q_0. C_Σ is the total capacitance of the dot. The second term, $E_{\text{int}}(N, S, M)$, is the sum of the energies of the occupied N-electron levels with total spin S and total angular momentum M accounting for the internal degrees of freedom of the QD. Other corrections to the many-body interactions are also included in $E_{\text{int}}(N, S, M)$. In the orthodox theory, the second term is neglected because the QD is assumed to relax quickly

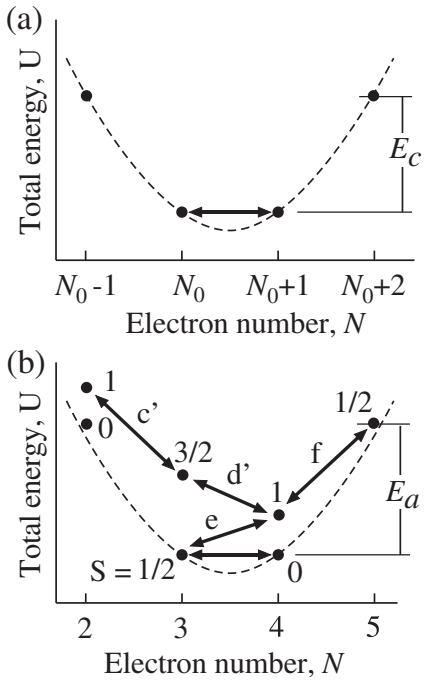

Figure 22. Total energy diagrams for (a) orthodox CB theory and (b) with long-lived ESs incorporated.

to the minimum energy, $E_{\rm int}^{(\rm min)}$, which is almost independent of N. In this SET scheme, an electron that has entered the island leaves before another electron is allowed to enter when $U(N_0) = U(N_0+1)$ as shown in figure 22(a). This situation is maintained unless the excitation energy exceeds the charging energy, $E_{\rm c} = e^2/C_{\sum}$. In this picture, long-lived spin states are neglected and only N-electron GSs only considered.

For a QD, in which energy quantization and many-body interactions are significant, we must consider the discrete energy of the dot, $E_{\rm int}(N, S, M)$. We focus on the regime where spin-flip energy relaxation is effectively absent. Since the momentum relaxation is effective, the QD can still easily relax to the minimum energy $E_{\rm int}(N, S)$. However, if the QD is excited to any N-electron state with a total spin different from that of the N-electron GS, the ES cannot always relax to the GS before the QD undergoes a tunnelling transition to another $(N \pm 1)$-electron state. Successive tunnelling transitions force the QD into highly non-equilibrium configurations. Figure 22(b) shows a particular $U(N, S)$ diagram, which can actually be realized in our QD (discussed below). Long-lived ESs are now included, and the different spin states have different energies because of the Coulomb interactions. The allowed tunnelling transitions indicated by the arrows require excitation energies smaller than the addition energy, $E_{\rm a}$. Here now, $E_{\rm c}$ is replaced with $E_{\rm a}$, which includes the N dependent $E_{\rm int}^{(\rm min)}$. All of these transitions can cause the dot state (N, S, and U) to fluctuate dramatically.

6.2. Transient current spectroscopy

To investigate the highly non-equilibrium transport, we employ the pulse excitation technique on a circular QD mesa introduced in section 3.2. One can only study the transient current

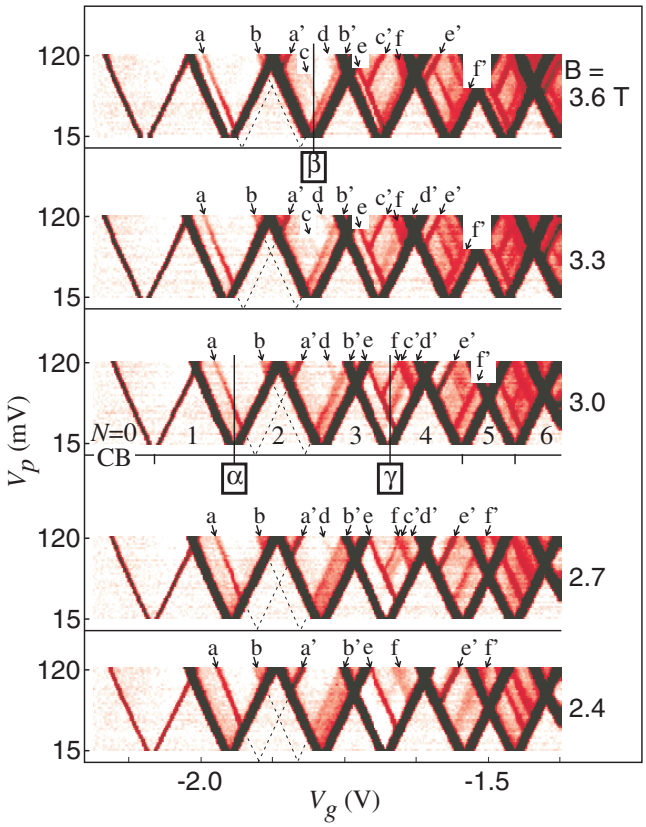

Figure 23. Pulse excited current spectra measured from $B = 2.4$ T (bottom) to 3.6 T (top). The tones represent current amplitudes (white (0 pA)—grey (red) (0.25 pA)—black ($\geqslant$0.5 pA)).

associated with long-lived spin states whose total spin is different from those of any lower-lying states. Therefore, only the lowest-energy state for a given N and S can be observed using the pulse excited current, and other short-lived states can be neglected.

Figure 23 shows the pulse excited current spectra for $N = 0$–6 at $B = 2.4$–3.6 T. For each B, a current peak initially observed in the absence of the pulse ($V_p \sim 0$) and representing a SET transition between N- and $(N + 1)$-electron GSs splits into two main peaks of equal height (truncated in the grey (colour) scale), when the pulse is applied. Weaker additional peaks, indicated by the arrows, are due to transient current through long-lived ESs. Rich structure is observed in the current spectra between 2 and 4 T since various many-body spin states are energetically close to each other [51]. The representative spectra in figure 23 are observed in the B range where the GS of the N-electron QD is not spin polarized, i.e., the smaller-S states have lower energy.

There are some general features observed in the spectra. Firstly, when the peak positions are extrapolated to lower V_p, pairs of peaks (e.g. the two labelled a and a′) generally meet at $V_p = 0$ exactly (see also the dashed line for pairs a–a′ and b–b′). This behaviour can be seen for all peaks over the entire magnetic field range (0–6 T) investigated. The peaks in figure 23 are labelled in such a way that the prime (non-prime) labelled peaks are associated with tunnelling transitions in the low- (high-) voltage state of the pulse. Secondly, some of the current peaks are terminated by other current peaks (e.g. peak d is terminated by peak b′, and

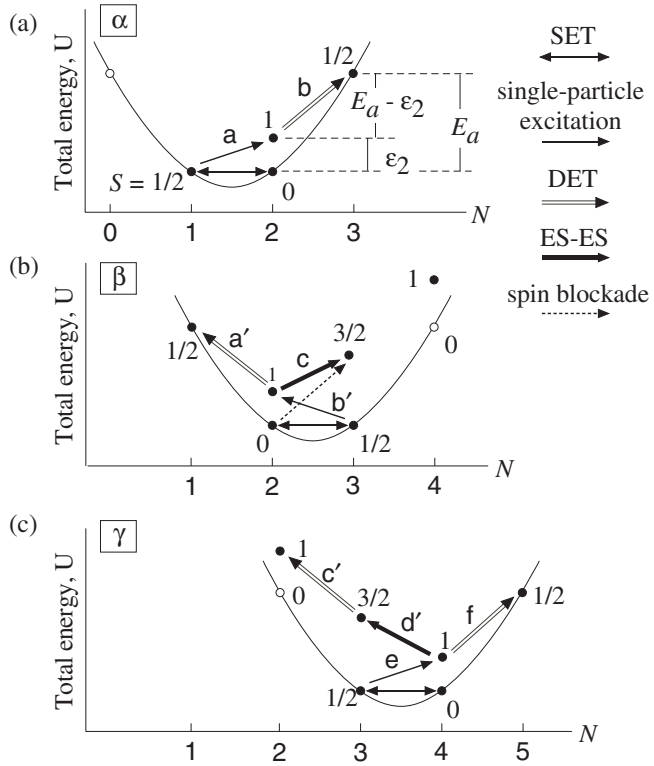

Figure 24. Total energy diagrams $U(N, S)$. (a)–(c) summarize tunnelling transitions respectively at gate voltages α, β, and γ in figure 23.

peak d′ by peak e), as discussed below. Thirdly, the number of peaks is more than that expected for a simple SET scheme. For example, as shown in figure 21, there are only two allowed tunnelling transitions between long-lived states in $N = 1$ and 2 QD. However, in total three peaks (a and b in addition to the original SET peak) are seen in the conducting region between the $N = 1$ and 2 CB regions. Peak b cannot be explained by a higher-lying short-lived ES of the $N = 2$ QD; it can only be explained by considering non-equilibrium tunnelling processes.

6.3. Breakdown of the single-electron tunnelling scheme

All the transport spectra in figure 23 can be well understood from the total energy diagrams in figure 24. Figure 24(a) is the $U(N, S)$ diagram when the gate voltage is set to position α at $B = 3.0$ T in figure 23. SET between $(N, S) = (1, 1/2)$ and $(2, 0)$ is always possible even at zero excitation energy. The single-particle excitation to $(2, 1)$, corresponding to peak a in figure 23, becomes possible when the excitation energy exceeds the level spacing, ε_2. Since the energy relaxation from $(2, 1)$ to $(2, 0)$ is forbidden due to spin conservation, the $(2, 1)$ state is stable until another tunnelling transition takes place. Then, the QD can be excited to charge state $(3, 1/2)$, as indicated by the double-line arrow in figure 24(a). This excitation requires the energy $E_a - \varepsilon_2$, which is considerably smaller than the addition energy E_a. Since the excitation to $(3, 1/2)$ involves three charge states, $N = 1$, 2, and 3, this tunnelling process can be thought of as a novel double-electron tunnelling (DET) mechanism. The corresponding current peak is labelled b in figure 23. At gate voltage α, this novel DET process would require

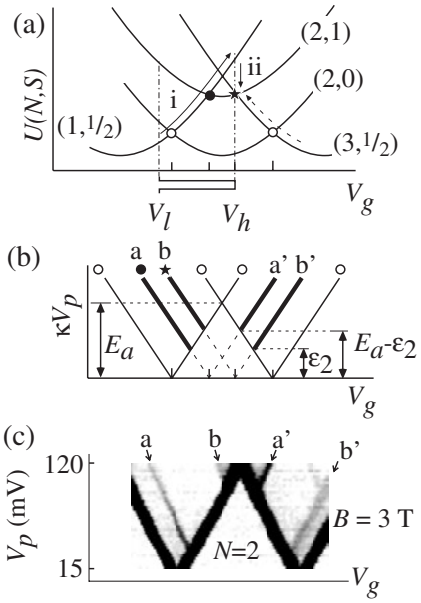

Figure 25. (a) The total energy diagram $U(N, S)$ as a function of the gate voltage. (b) Conditions for normal SET, excitation to the $(N, S) = (2, 1)$ state, and the double-electron tunnelling. (c) The pulse excited current spectrum at $B = 3$ T near the $N = 2$ CB region.

$V_p \approx 200$ mV, which is outside the range of figure 23. However, it is clear that peak b appears inside the region where SET is expected from orthodox theory.

In order to fully describe the tunnelling transition during pulses, $U(N, S)$ is plotted against V_g in figure 25(a). The normal SET tunnelling (GS–GS tunnelling) current peaks occur at level crossings labelled ∘, whilst transient current appearing at higher-energy level crossings are denoted with different symbols. Suppose a V_g pulse is applied as shown. The state is initially $(1, \frac{1}{2})$ in the low-voltage state of the pulse ($V_g = V_l$). $U(1, \frac{1}{2})$ is raised to a higher energy (arrow i) when the high voltage is applied ($V_g = V_h$), and subsequent inelastic tunnelling results in either the $(2, 0)$ or the $(2, 1)$ state. If it is $(2, 1)$ (arrow ii), it is now possible for another electron to be transported at the crossing $U(2, 1) = U(3, \frac{1}{2})$ marked by ⋆. In this case transient transport persists until the inelastic tunnelling transition from $(3, \frac{1}{2})$ to $(2, 0)$ occurs, because spin-flip energy relaxation from $(2, 1)$ to $(2, 0)$ is absent. The QD returns back to the initial state $(1, \frac{1}{2})$ when the pulse is switched to V_l. This new tunnelling process involves three charge states, so this is why we refer to it as DET. Conventional DET, within the orthodox CB theory, appears only for $\kappa V_p \geqslant E_a$ [13, 24], while the novel DET here takes place even for $\kappa V_p < E_a$. Here κ is the conversion factor when changing from gate voltage to energy. This novel DET process should appear on the thick line b in the κV_p–V_g plane of figure 25(b). The novel DET is clearly seen in the experimental data of figure 25(c) as indicated by line b. We emphasize that this peak cannot be due to regular SET involving higher-lying $N = 2$ ESs. The pulse measurement successfully allows us to identify the extra peak b as a novel DET feature.

Transient current can also appear in the low-voltage state of the pulse. If a pulse is applied to excite the QD along $(3, \frac{1}{2})$ in the direction of more negative V_g (the dashed arrow in figure 25(a)), GS–ES tunnelling between $(3, \frac{1}{2})$ and $(2, 1)$ should appear along the line b′ in figure 25(b). Similarly, novel DET appears at the crossing $U(2, 1) = U(1, \frac{1}{2})$ (corresponding

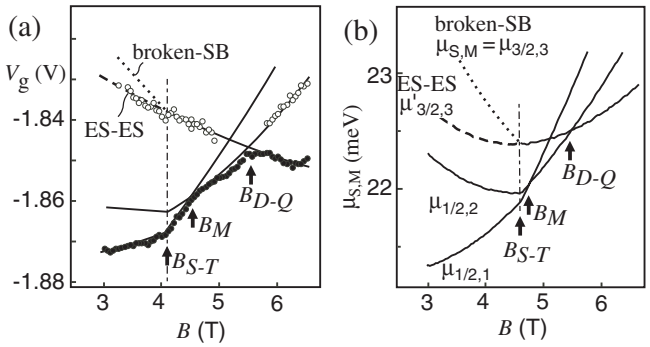

Figure 26. (a) The gate voltage dependence of the pulse excited current peaks. Solid curves are guides to the eye. (b) The electrochemical potential, $\mu_{S,M}$, calculated by means of exact diagonalization for tunnelling transitions to ($N = 3$, S, M) states.

to feature a′). Note that the extrapolated lines a and a′ (b and b′) meet at zero excitation energy. These features are clearly seen in figure 25(c) as well as over the whole B range in figure 23.

6.4. The spin blockade effect and related non-equilibrium transport

We now discuss spin blockade and associated non-equilibrium transport. The tunnelling transition between $N = 2$ and 3 is the first case where spin blockade appears. Figure 24(b) shows the $U(N, S)$ diagram when the gate voltage is adjusted to β at $B = 3.6$ T in figure 23. The SET between the $N = 2$ and 3 GSs, single-particle excitation to $(N, S) = (2, 1)$ (transition b′ in figure 24(b) and the corresponding peak b′ in figure 23), and novel double-electron tunnelling into $(1, 1/2)$ (labelled by a′) are clearly seen. The extra peak c, although it is faint in figure 23, is attributed to the transition from $(2, 1)$ to $(3, 3/2)$. We call this tunnelling process ES–ES tunnelling, because it is between the $N = 2$ ES and 3 ES with no GSs involved. This highly non-equilibrium transport process is possible because the spin-flip energy relaxation from $(2, 1)$ to $(2, 0)$ is forbidden. Since this ES–ES excitation requires a 'pre-excitation' from $(3, 1/2)$ to $(2, 1)$ (labelled b′), transition c only appears when transition b′ is possible. So the corresponding current peak, c in figure 23, is terminated by peak b′. Similar 'terminations', such as peak d terminated by peak b′, peak c′ by peak e, and peak d′ by peak e, are clearly seen in figure 23. They are all attributed to ES–ES tunnelling.

It should be noted that the transition from $(2, 0)$ to $(3, 3/2)$ which changes S by $3/2$ is not observed because of spin blockade. This is confirmed by close observation of the B dependence of peak c. In the following, we show that peak c is attributed to ES–ES tunnelling from $(2, 1)$, and not to the broken spin blockaded transition from $(2, 0)$. Figure 26(a) shows the B dependence of the peak positions for SET between the $N = 2$ and 3 GSs (solid circles), and for one of the pulse excited current peaks (open circles) [52]. The complete current spectrum is shown in figure 12(b). The peak of interest, c, corresponds to the open circles for between 3 and 4 T in figure 26(a). The position of the solid circles shows some kinks that are related to the level crossings of the $N = 2$ or 3 GSs. From a comparison with an exact diagonalization calculation shown in figure 26(b), we can identify a transition from a spin singlet $(N, S, M) = (2, 0, 0)$ to a spin triplet $(2, 1, 1)$ of the $N = 2$ QD at $B = B_{S-T}$, a momentum transition from $(3, 1/2, 1)$ to $(3, 1/2, 2)$ of the $N = 3$ QD at $B = B_M$, and a transition from the spin doublet $(3, 1/2, 2)$ to spin quadruplet $(3, 3/2, 3)$ of the $N = 3$ QD at $B = B_{D-Q}$. Each transition field is indicated by an arrow. The long-lived ESs (open

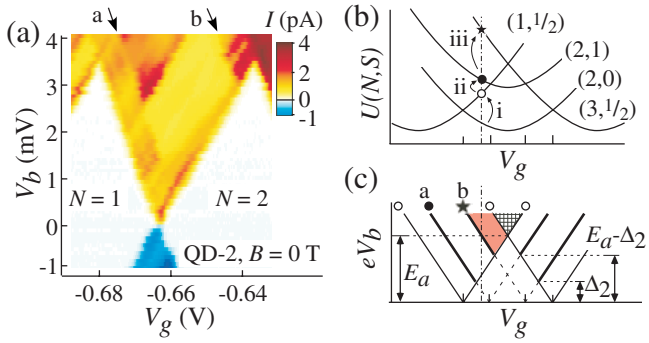

Figure 27. (a) A greyscale (colour) plot of the dc in the V_b–V_g plane. (b) The total energy diagram for dc excitation processes. (c) Corresponding conditions for dc excitation transport.

circles) follow the crossing behaviour with respect to the doublet–quadruplet GS transition at around $B \sim B_{D-Q}$, indicating that the ES peak for $B < B_{D-Q}$ arises from the transition between (2, 1, 1) and (3, 3/2, 3). This transition is just a GS($N = 2$)–ES($N = 3$) transition for $B_{S-T} < B < B_{D-Q}$. Now suppose we look at the peak position for $B < B_{S-T}$. If the current arises from the transition from (2, 0, 0) to (3, 3/2, 3), so violating spin blockade, the peak position should show a kink at $B = B_{S-T}$ due to the GS level crossing of the $N = 2$ QD, and follow the dotted line in figures 26(a) and (b). However, the peak position does not show any kink at $B \sim B_{S-T}$, and follows the dashed line smoothly to lower B. This is expected only for the ES–ES tunnelling transition between (2, 1, 1) and (3, 3/2, 3). Therefore, this current peak for $B < B_{S-T} \sim 4$ T must be associated with ES–ES tunnelling. Actually, we never see the spin blockaded transition with our current sensitivity (∼10 fA).

6.5. More complex excitations

Other complex tunnelling processes involving both novel DET and ES–ES tunnelling are also observed. Peak d (c′) in figure 23, which is terminated by peak b′ (e), is also attributed to ES–ES tunnelling, whose excitation process involves three charge states. More complicated excitations are expected for QDs with more electrons. Four different peaks (e, f, c′ and d′ in figure 23) are observed at $B = 3$ T between the $N = 3$ and 4 CB regions. The corresponding transitions are indicated in the total energy diagram in figure 24(c). The fluctuation in the total energy can be significantly greater than the pulse excitation energy. Non-equilibrium transport can lead to the accumulation of energy in excess of the excitation energy. As N increases, many long-lived ESs with different S can contribute to the transport. The complexity of many-body excitations is expected to increase with N and S [53].

6.6. Non-equilibrium transport in the dc measurement

Although the above non-equilibrium transport characteristics are deduced from pulse measurements, we expect to see similar features in conventional dc excitation measurements. For example, figure 27(a) shows the dc spectrum for between the $N = 1$ and 2 CB regions at $B = 0$ T. In addition to the expected current step marked by arrow a, associated with excitation to the ES(N, S) = (2, 1), we see an extra current step marked by arrow b that we associate with the novel DET.

The novel DET involving $N = 1$, 2, and 3 is allowed in dc measurements when eV_b is greater than $|U(1, \frac{1}{2}) - U(2, 0)|$ (the energy required for normal SET between the $N = 1$ and

2 GSs; arrow i in figure 27(b)), $|U(2, 1) - U(1, \frac{1}{2})|$ (the excitation energy to the $N = 2$ spin triplet ES from the $N = 1$ GS; arrow ii), and $|U(3, \frac{1}{2}) - U(2, 1)|$ (the extra energy for novel DET; arrow iii). The necessary conditions for the novel DET here are satisfied in the grey (red) region in the eV_b–V_g plane of figure 27(c). The condition in dc measurement for novel DET, as well as the other tunnelling processes, is equivalent to that in pulse measurements, obtained by replacing κV_p with eV_b.

7. Summary

We have described inelastic spin relaxation and related non-equilibrium transport in the CB regime by means of pulse excited tunnelling current measurements. The electrical pump and probe techniques used to perform transient current spectroscopy have successfully revealed the relaxation time and tunnelling rates separately. The relaxation dynamics in lateral and vertical QDs can be explained well in terms of allowed transitions and forbidden transitions, in analogy with real atoms.

We believe that our pulse techniques can be extended to observe and to manipulate coherency of spin and momentum in a QD. Coherent manipulation of charge states in a superconducting island has been investigated by a similar technique [54]. We expect to perform similar coherent manipulation in a QD system, in which an electron goes back and forth between two coupled QDs. Then we can probably investigate decoherence of the system. Since the decoherence time is always shorter than the energy relaxation time, the decoherence time for the momentum degree of freedom in a QD cannot exceed the inelastic momentum relaxation time, which is 3–10 ns in our QD. However, the spin decoherence time is expected to be much longer. Spin coherency can be measured by electron spin resonance techniques on applying a microwave magnetic field in the presence of a static magnetic field [55]. By combining with the pump and probe scheme introduced in this article, initialization, manipulation, and measurement processes can be separated, and this is desirable for quantum information technology.

Acknowledgments

Discussions with R Aguado, T Honda, K Ishibashi, A V Khaetskii, L P Kouwenhoven, Y Nakamura, T H Oosterkamp, W G van der Wiel are gratefully acknowledged.

References

[1] Awschalom D D, Loss D and Samarth N (ed) 2002 *Semiconductor Spintronics and Quantum Computation* (Berlin: Springer)
[2] Loss D and DiVincenzo D P 1998 *Phys. Rev.* A **57** 120
[3] Kouwenhoven L P, Marcus C M, McEuen P L, Tarucha S, Westervelt R M and Wingreen N S 1997 *Mesoscopic Electron Transport* (*NATO ASI Series E, vol 345*) ed L L Sohn, L P Kouwenhoven and G Schön (Dordrecht: Kluwer–Academic) pp 105–214
[4] Tarucha S, Austing D G, Honda T, van der Hage R J and Kouwenhoven L P 1996 *Phys. Rev. Lett.* **77** 3613
[5] Kouwenhoven L P, Oosterkamp T H, Danoesastro M W S, Eto M, Austing D G, Honda T and Tarucha S 1997 *Science* **278** 1788
[6] Ciorga M, Wensauer A, Pioro-Ladriere M, Korkusinski M, Kyriakidis J, Sachrajda A S and Hawrylak P 2002 *Phys. Rev. Lett.* **88** 256804
[7] Sasaki S, De Franceschi S, Elzerman J M, van der Wiel W G, Eto M, Tarucha S and Kouwenhoven L P 2000 *Nature* **405** 764
[8] Khaetskii A V and Nazarov Yu V 2000 *Physica* E **6** 470
[9] Fabian J and Das Sarma S 1999 *J. Vac. Sci. Technol.* B **17** 1708

[10] Pikus G E and Titkov A N 1984 *Optical Orientation* ed F Meier and B P Zakharchenya (Amsterdam: Elsevier) pp 73–131
[11] Kikkawa J M and Awschalom D D 1998 *Phys. Rev. Lett.* **80** 4313
[12] Paillard M, Marie X, Renucci P, Amad T, Jbeli A and Gerard J M 2001 *Phys. Rev. Lett.* **86** 1634
[13] Grabert H and Devoret M H (ed) 1991 *Single Charge Tunneling, Coulomb Blockade Phenomena in Nanostructures* (*NATO ASI Series B, vol 294*) (New York: Plenum)
[14] Fujisawa T, Tokura Y and Hirayama Y 2001 *Physica* B **298** 573
[15] Weis J, Haug R J, von Klitzing K and Ploog K 1993 *Phys. Rev. Lett.* **71** 4019
[16] Fujisawa T, Austing D G, Hirayama Y and Tarucha S 2003 *Japan. J. Appl. Phys.* at press
[17] Akera H 1999 *Phys. Rev.* B **60** 10683
[18] Hayashi T, Fujisawa T and Hirayama Y 2003 *Phys. Status Solidi* at press
[19] Fujisawa T, Tokura Y and Hirayama Y 2001 *Phys. Rev.* B **63** 081304(R)
[20] Bockelmann U 1994 *Phys. Rev.* B **50** 17271
[21] Khaetskii A V and Nazarov Yu V 2000 *Phys. Rev.* B **61** 12639
[22] Fujisawa T, Oosterkamp T H, van der Wiel W G, Broer B W, Aguado R, Tarucha S and Kouwenhoven L P 1998 *Science* **282** 932
[23] van der Vaart N C, Godijn S F, Nazarov Yu V, Harmans C J P M and Mooij J E 1995 *Phys. Rev. Lett.* **74** 4702
[24] Kouwenhoven L P, Austing D G and Tarucha S 2001 *Rep. Prog. Phys.* **64** 701
[25] Tarucha S, Honda T, Austing D G, Tokura Y, Muraki K, Oosterkamp T H, Janssen J W and Kouwenhoven L P 1998 *Physica* E **3** 112
[26] Fujisawa T, Austing D G, Tokura Y, Hirayama Y and Tarucha S 2002 *Nature* **419** 278
[27] Matagne P, Leburton J P, Austing D G and Tarucha S 2002 *Phys. Rev.* B **65** 085325
[28] Tokura Y, Sasaki S, Austing D G and Tarucha S 2001 *Physica* B **298** 260
[29] Benisty H 1995 *Phys. Rev.* B **51** 13281
[30] Heitz R, Born H, Guffarth F, Stier O, Schliwa A, Hoffmann A and Bimberg D 2001 *Phys. Rev.* B **64** 241305
[31] Urayama J, Norris T B, Singh J and Bhattacharya P 2001 *Phys. Rev. Lett.* **86** 4930
[32] Malik S, Le Ru E V, Childs D and Murray R 2001 *Phys. Rev.* B **63** 155313
[33] Seeger K 1985 *Semiconductor Physics: an Introduction* (Berlin: Springer) pp 153–213
[34] Bockelmann U and Bastard G 1990 *Phys. Rev.* B **42** 8947
[35] Averin D V and Nazarov Yu V 1991 *Single Charge Tunneling, Coulomb Blockade Phenomena in Nanostructures* (*NATO ASI Series B, vol 294*) ed H Grabert and M H Devoret (New York: Plenum) pp 217–48
[36] Eto M 2001 *Japan. J. Appl. Phys.* 1 **40** 1929
[37] Sukhorukov E V, Burkard G and Loss D 2001 *Phys. Rev.* B **63** 125315
[38] De Franceschi S, Sasaki S, Elzerman J M, van der Wiel W G, Tarucha S and Kouwenhoven L P 2001 *Phys. Rev. Lett.* **86** 878
[39] Bychkov Yu A and Rashba E I 1984 *JETP Lett.* **39** 78
[40] Halperin W P 1986 *Rev. Mod. Phys.* **58** 533
[41] Recher P, Sukhorukov E V and Loss D 2000 *Phys. Rev. Lett.* **85** 1962
[42] Hanson R, Witkamp B, Vandersypen L M K, Willems van Beveren L H, Elzerman J M and Kouwenhoven L P 2003 *Preprint* cond-mat/0303139
[43] Seck M, Potemski M and Wyder P 1997 *Phys. Rev.* B **56** 7422
[44] Gupta J A, Knobel R, Samarth N and Awschalom D D 2001 *Science* **292** 2458
[45] Kavokin K V 2001 *Phys. Rev.* B **64** 075305
[46] Bethe H A and Salpeter E E 1957 *Quantum Mechanics of One- and Two-Electron Atoms* (Berlin: Springer)
[47] Weinmann D, Häusler W and Kramer B 1995 *Phys. Rev. Lett.* **74** 984
[48] Ciorga M, Sachrajda A S, Hawrylak P, Gould C, Zawadzki P, Jullian S, Feng Y and Wasilewski Z 2000 *Phys. Rev.* B **61** R16315
[49] Fujisawa T, Austing D G, Tokura Y, Hirayama Y and Tarucha S 2002 *Phys. Rev. Lett.* **88** 236802
[50] Agam O, Wingreen N S, Altshuler B L, Ralph D C and Tinkham M 1997 *Phys. Rev. Lett.* **78** 1956
[51] Fujisawa T, Tokura Y, Austing D G, Hirayama Y and Tarucha S 2002 *Physica* B **314** 224
[52] Fujisawa T, Austing D G, Tokura Y, Hirayama Y and Tarucha S 2002 *Proc. Int. Conf. on Physics of Semiconductors* ed A R Long and J H Davies, *IOP Conf. Ser.* **171** 245
[53] Altshuler B L *et al* 1997 *Phys. Rev. Lett.* **78** 2803
[54] Nakamura Y, Pashkin Yu A and Tsai J S 1999 *Nature* **398** 786
[55] Engel H A and Loss D 2001 *Phys. Rev. Lett.* **86** 4648